

AMUSE: Anytime Muon with Stable Gradient Evaluation

Jueun Kim *
KAIST
jueunkim@kaist.ac.kr


Baekrok Shin *
KAIST
br.shin@kaist.ac.kr

Jihun Yun
KRAFTON
jihuny@krafton.com

Beomhan Baek
Seoul National University, KRAFTON
bhbaek2001@snu.ac.kr

Minhak Song
KAIST, KRAFTON
minhaksong@kaist.ac.kr

Chulhee Yun
KAIST
chulhee.yun@kaist.ac.kr

 <https://github.com/kjeiun/amuse>

Abstract

Modern deep learning commonly relies on AdamW with prescribed learning rate schedules, but recent works challenge both components: Schedule-Free optimization removes explicit schedules via iterate averaging, and Muon improves the update geometry by orthogonalizing momentum for matrix parameters. Despite Muon’s strong empirical performance, its underlying mechanism remains partially understood. We study Muon through the river-valley loss landscape, where useful training progress occurs along a flat, low-curvature bulk subspace (the river), while high-curvature dominant directions form steep valley walls that induce oscillations. We empirically show that while Muon’s orthogonalization accelerates river progress by increasing the bulk component, it also amplifies dominant-direction noise, causing oscillatory trajectories. Building on this, we propose Anytime MUon with Stable gradient Evaluation (AMUSE), which integrates Muon’s rapid bulk progress with the stabilizing effect of Schedule-Free averaging. AMUSE uses a time-varying interpolation coefficient that initially evaluates gradients near the fast Muon sequence for rapid adaptation, then gradually shifts toward the stable averaged sequence to suppress valley-wall oscillations. As a result, AMUSE requires no learning rate schedules and supports anytime training. Across vision tasks and large language model pretraining, AMUSE consistently improves the performance-iteration Pareto frontier over (Schedule-Free) AdamW and Muon.

1 Introduction

Optimization remains a primary lever for improving training efficiency in deep learning. For many modern architectures, especially Transformer-based language models, the standard recipe has long combined the Adam(W) optimizer (Kingma and Ba, 2015; Loshchilov and Hutter, 2019) with warmup and a prescribed learning rate decay schedule such as cosine decay (Loshchilov and Hutter, 2017).

Recent work challenges both components of this recipe. Schedule-Free AdamW (Defazio et al., 2024) removes the need for explicit learning rate schedules by evaluating gradients at interpolated points between the current and averaged iterates, while using the averaged iterate for inference. It has shown strong empirical performance relative to schedule-based baselines, including winning the Self-Tuning track of the 2024 AlgoPerf Challenge (Dahl et al., 2023; Kasimbeg et al., 2025).

*Authors contributed equally to this paper.

A complementary advance changes the underlying geometry of the update itself. Muon (Jordan et al., 2024) exploits matrix structure by applying momentum to matrix-valued parameters and orthogonalizing the resulting update direction. Muon and its variants have been reported to outperform AdamW in language model pretraining (Liu et al., 2025a), and have recently been adopted in large-scale open-model training recipes, including Kimi-K2 (Kimi Team, 2025), GLM-5 (GLM-5 Team, 2026), and DeepSeek-V4 (DeepSeek-AI, 2026). Despite this empirical success, *why orthogonalized momentum improves optimization* remains only partially understood.

We take this question as the first step toward optimizer design, and analyze Muon from the perspective of loss landscape geometry. Deep learning optimization takes place in high-dimensional parameter spaces whose loss landscapes are highly anisotropic. Empirically, the Hessian spectrum often contains a small number of large outlier eigenvalues and a much larger bulk of relatively small eigenvalues. This spectral structure induces a local decomposition of the parameter space into a low-dimensional, high-curvature *dominant subspace* and a high-dimensional, low-curvature *bulk subspace* (Ghorbani et al., 2019; Pappan, 2018, 2019, 2020; Sagun et al., 2016, 2017).

Recent work casts this anisotropy as the *river-valley landscape* (Song et al., 2025a; Wen et al., 2025): the dominant subspace forms steep valley walls, while the bulk subspace forms a relatively flat river. In this picture, training progress occurs mainly along the river, whereas dominant subspace components cause valley-wall oscillations. This suggests two core principles for optimizer design: (i) take large, consistent steps along the river and (ii) suppress unnecessary updates across the valley.

We find that Muon naturally promotes the first part of this principle. By orthogonalizing the momentum matrix, Muon prevents the update from being dominated by a few large singular components, producing a more balanced matrix-valued step. Empirically, Muon updates contain substantially larger bulk components than SGD or Adam. Moreover, orthogonalization itself explicitly increases this relative bulk component. This provides a geometric explanation for Muon’s efficiency: *orthogonalized momentum accelerates progress along the river directions*.

However, this benefit comes with a tradeoff. Because orthogonalization is not selective, it can amplify noisy components as well as useful ones. In particular, small noise aligned with high-curvature dominant directions can become oscillations across the valley walls after orthogonalization, leading to less stable trajectories (He et al., 2025; Qi et al., 2026; Zhang et al., 2026a).

Schedule-Free (SF) optimization offers a complementary stabilizing mechanism by evaluating gradients at an interpolation between the fast optimizer sequence and an averaged inference sequence. Song et al. (2025b) show that this mechanism can keep the inference trajectory close to the river without requiring learning rate decay. We find this particularly beneficial for Muon: evaluating gradients closer to the averaged sequence reduces the high-curvature component before orthogonalization, thereby suppressing oscillations between the valley walls and stabilizing the resulting trajectory.

Motivated by this complementarity, we propose **AMUSE** (Anytime MUon with Stable gradient Evaluation). AMUSE combines Muon’s orthogonalized matrix updates with the SF formulation, using a *time-varying* interpolation coefficient. AMUSE initially evaluates gradients near the fast Muon sequence for rapid adaptation, then gradually shifts toward the averaged sequence, where gradients are less dominated by high-curvature components. Because this schedule is independent of the total training horizon and requires no learning rate decay, AMUSE naturally supports *anytime* training.

We evaluate AMUSE across a diverse set of benchmarks spanning image classification, segmentation, and large language model pretraining. The results show that AMUSE consistently improves the performance-iteration Pareto frontier over (Schedule-Free) AdamW and Muon. Notably, AMUSE reaches Muon’s final performance with 1.51 \times , 1.12 \times , and 3.08 \times fewer steps on 720M LLM pretraining, ImageNet with ResNet-50, and ImageNet with ViT fine-tuning, respectively.

2 Related Work

2.1 River-Valley Loss Landscape

Previous studies have characterized neural network training through a low-rank Hessian structure, consisting of a few high-curvature directions and a much broader bulk component (Ghorbani et al., 2019; Pappayan, 2018, 2019, 2020; Sagun et al., 2016, 2017; Yao et al., 2020). Recent work further interprets this geometry through the river-valley landscape (see Figure 1 for illustration), where dominant directions form steep valley walls while the bulk defines the flatter river floor where most useful progress occurs (Belloni et al., 2025; Cohen et al., 2025; Deng et al., 2026; Song et al., 2025a; Wang et al., 2025, 2024; Wen et al., 2025; Zhou et al., 2025).

Wen et al. (2025) use this geometry to explain the success of Warmup-Stable-Decay (WSD) schedules in large language model pretraining: the stable phase facilitates rapid traversal along the river, while the decay phase helps the iterate settle onto the valley floor. Extending this perspective, Belloni et al. (2025) show that a similar geometry also arises in convolutional networks trained on image classification tasks. Song et al. (2025a) show that projecting updates only onto the dominant subspace is insufficient to reduce training loss, while updates projected onto the bulk subspace remain effective. Recently, several works have leveraged the river-valley landscape to design optimizers that either amplify updates along river directions or stabilize oscillations along valley directions (Liu et al., 2025b; Luo et al., 2026; Zhang et al., 2026b; Zhu et al., 2026).

2.2 Schedule-Free Optimizer

Defazio et al. (2024) introduce the schedule-free (SF) optimizer as an interpolation between Polyak–Ruppert (PR) averaging (Polyak and Juditsky, 1992; Ruppert, 1988) and primal averaging (Nesterov, 2009; Tao et al., 2018). Its update is given by

$$\begin{aligned} \mathbf{y}_t &= (1 - \beta)\mathbf{z}_t + \beta\mathbf{x}_t, \\ \mathbf{z}_{t+1} &= \mathbf{z}_t - \eta\Delta_t, \\ \mathbf{x}_{t+1} &= (1 - c_{t+1})\mathbf{x}_t + c_{t+1}\mathbf{z}_{t+1}, \end{aligned} \tag{1}$$

where η is the learning rate, Δ_t is the base optimizer update computed from the gradient at \mathbf{y}_t , $c_{t+1} = 1/(t+1)$, and the initialization satisfies $\mathbf{z}_1 = \mathbf{x}_1$. The framework can be combined with different base optimizers through the choice of Δ_t . For example, defining Δ_t as a stochastic gradient at \mathbf{y}_t gives SF-SGD, whereas computing Δ_t using an RMSProp update with decoupled weight decay gives SF-AdamW.

The three sequences play distinct roles: \mathbf{y}_t is the gradient evaluation point, \mathbf{z}_t is the primary iterate that follows the base optimizer update, and \mathbf{x}_t is the averaged sequence used for inference. The interpolation parameter β controls whether gradient evaluation tracks the fast-moving base trajectory (\mathbf{z}_t) or the more stable averaged trajectory (\mathbf{x}_t), thereby balancing rapid adaptation and stability. Under this formulation, SF optimizers are known to achieve a performance–time Pareto frontier, as evidenced by winning the Self-Tuning track of the 2024 AlgoPerf Challenge (Dahl et al., 2023).

Song et al. (2025b) later connect the empirical success of SF optimization to the river-valley landscape, showing that, with an appropriate choice of β , the inference trajectory \mathbf{x}_t of SF-AdamW follows the river throughout training. Their findings suggest that the implicit averaging in SF optimizer filters out high-curvature fluctuations from the valley walls. As a result, SF optimizer can remain near the river without requiring an explicit decay phase or an additional average of the model parameters.

2.3 Muon Optimizer

Muon (Jordan et al., 2024) is a recently introduced optimizer that leverages matrix structure by orthogonalizing matrix-valued updates. At each iteration t , given a matrix \mathbf{W}_t and its gradient \mathbf{G}_t , the updates are defined as:

$$\begin{aligned} \mathbf{M}_t &= \mu\mathbf{M}_{t-1} + \mathbf{G}_t, \\ \mathbf{W}_{t+1} &= \mathbf{W}_t - \eta\mathcal{O}(\mathbf{M}_t), \end{aligned} \tag{2}$$

where η is the learning rate, μ is the momentum coefficient, and \mathcal{O} denotes an orthogonalization operator, which is approximated using a Newton-Schulz iteration (Bernstein and Newhouse, 2024) for computational efficiency.

For non-matrix-valued parameters, including embeddings and classification heads, updates are instead performed using standard optimizers such as SGD or Adam(W).

Recent theoretical studies have begun to explain Muon’s rapid convergence through the normalization effect of its matrix-wise orthogonalization, especially in ill-conditioned settings. Shen et al. (2025) show that Muon can be advantageous when neural network Hessians exhibit low-rank or structured spectral geometry, while Ma et al. (2026) show that its orthogonalization can act as an effective preconditioner, yielding condition-number-free linear convergence in matrix factorization and linear transformer settings. Other recent studies further show that Muon’s orthogonalized updates induce balanced component learning (Kang et al., 2026), improving minority-group performance in imbalanced settings (Vasudeva et al., 2026). However, this same mechanism can also strengthen noisy components, potentially leading to less stable dynamics (Qi et al., 2026; Zhang et al., 2026b).

3 A River-Valley Analysis of Muon and Schedule-Free Dynamics

In this section, we analyze Muon and Schedule-Free dynamics in controlled deep learning settings where the leading Hessian eigenspaces can be computed directly. We first define the dominant and bulk subspaces used in our measurements. Section 3.1 then shows that Muon produces more bulk-oriented updates than SGD or AdamW, but that orthogonalization can also amplify small components in the dominant subspace, inducing oscillations across the valley walls. Section 3.2 shows that Schedule-Free averaging mitigates this effect by evaluating gradients at points with smaller dominant components before orthogonalization.

Dominant & bulk decomposition. Following Song et al. (2025a), we decompose parameter-space directions using the Hessian eigenspaces of the loss $\mathcal{L} : \mathbb{R}^d \rightarrow \mathbb{R}$.

Definition 3.1 (Dominant and bulk subspaces). Let $\nabla^2 \mathcal{L}(\theta) \in \mathbb{R}^{d \times d}$ have eigenvalues $\lambda_1 \geq \dots \geq \lambda_d$ with corresponding eigenvectors $\mathbf{u}_1(\theta), \dots, \mathbf{u}_d(\theta)$. The top- k dominant subspace is $\mathcal{S}_k(\theta) := \text{span}\{\mathbf{u}_1(\theta), \dots, \mathbf{u}_k(\theta)\}$, and its orthogonal complement $\mathcal{S}_k^\perp(\theta)$ is the bulk subspace.

Definition 3.2 (Subspace projections). We define the projection matrix onto $\mathcal{S}_k(\theta)$ as $\mathbf{P}_k(\theta) := \sum_{i=1}^k \mathbf{u}_i(\theta) \mathbf{u}_i(\theta)^\top$, and the projection matrix onto $\mathcal{S}_k^\perp(\theta)$ as $\mathbf{P}_k^\perp(\theta) := \mathbf{I} - \mathbf{P}_k(\theta)$. For any nonzero vector $\mathbf{v} \in \mathbb{R}^d$, we define

$$r^{\text{dom}}(\mathbf{v}; \theta) = \frac{\|\mathbf{P}_k(\theta)\mathbf{v}\|_2}{\|\mathbf{v}\|_2}, \quad r^{\text{bulk}}(\mathbf{v}; \theta) = \frac{\|\mathbf{P}_k^\perp(\theta)\mathbf{v}\|_2}{\|\mathbf{v}\|_2}. \quad (3)$$

These quantities measure how strongly \mathbf{v} is aligned with the dominant and bulk subspaces, respectively. Since $\mathbf{P}_k(\theta)$ and $\mathbf{P}_k^\perp(\theta)$ are orthogonal projections, the ratios satisfy $(r^{\text{dom}})^2 + (r^{\text{bulk}})^2 = 1$; hence, we report r^{dom} in most measurements. Following Song et al. (2025a), we set k to the number of classes, motivated by prior observations that classification Hessians exhibit exactly this many outlier eigenvalues (Papayan, 2018, 2019).

Before analyzing Muon’s update decomposition, we verify that the dominant and bulk subspaces play distinct optimization roles in our controlled settings. Following Zhou et al. (2025), we independently scale the dominant and bulk components of each Muon update. As shown in Appendix B.3, amplifying the *bulk component* accelerates training, whereas amplifying the *dominant component* can destabilize optimization. This supports the river-valley interpretation in our setting and motivates the dominant/bulk update-ratio analysis below.

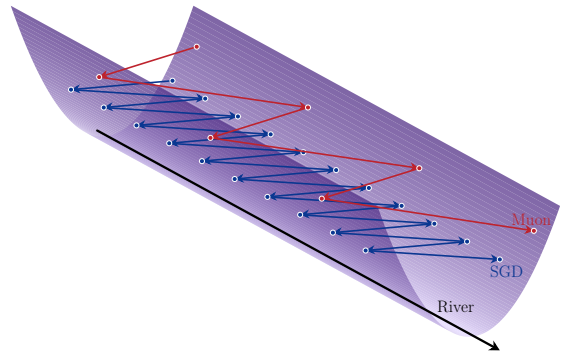


Figure 1: Illustration of a river-valley landscape. SGD oscillates across the valley walls and progresses slowly along the river, while Muon advances faster but remains oscillatory.

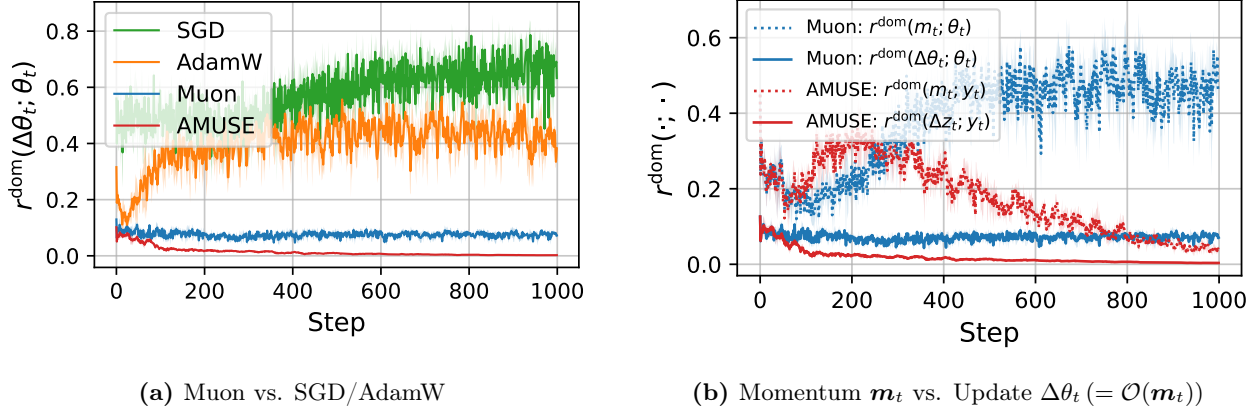


Figure 2: Comparison of dominant component ratios. Evaluated on a 5k MNIST subset using a 3-layer MLP. (a) Muon consistently produces smaller dominant updates than SGD/AdamW, and AMUSE further suppresses the dominant component. (b) Orthogonalization reduces Muon’s dominant ratio compared to momentum \mathbf{m}_t ; in contrast, AMUSE maintains low dominant ratios throughout, reflecting more stable gradient dynamics. Averaged over three runs.

3.1 Orthogonalization Makes Muon Updates More Bulk-Oriented

Muon applies an orthogonalization operator $\mathcal{O}(\cdot)$ to the momentum matrix M_t . Although this operation acts on the singular-vector geometry of each matrix, we measure its effect in the Hessian eigenspace by projecting the flattened update onto the dominant and bulk subspaces.

Figure 2a compares the dominant ratios of optimizer updates. Muon produces much smaller dominant-subspace components than SGD or AdamW, indicating that its updates are less aligned with the high-curvature directions and more oriented toward the bulk subspace. The figure also includes AMUSE, introduced in Section 4, as a preview of the stabilized variant of Muon; its updates have even smaller dominant ratios.

Figure 2b isolates the role of orthogonalization by comparing the raw momentum \mathbf{m}_t with the post-orthogonalized update $\Delta\theta_t (= \mathcal{O}(\mathbf{m}_t))$. For Muon, orthogonalization sharply reduces the dominant ratio relative to the raw momentum, showing that the orthogonalization step itself shifts the update away from dominant directions and toward the bulk subspace. This provides a geometric explanation for Muon’s effectiveness: by increasing the relative bulk component, *orthogonalized momentum promotes faster progress along the river directions*, where long-term learning takes place.

However, this normalization process prevents dominant components from dying out. Even a small residual dominant component can induce motion along high-curvature directions, leading to oscillations across the valley walls. This behavior resembles normalized-update dynamics, which can oscillate even on simple quadratic objectives (Arora et al., 2022); see Appendix A for an example.

3.2 Schedule-Free Stabilizes Muon Trajectories

The previous subsection shows that Muon produces large bulk movement, but its orthogonalized updates may also amplify valley-wall oscillations. Prior work has shown that, with an appropriate choice of β , the averaged trajectory \mathbf{x}_t of SF-AdamW follows the river (Song et al., 2025b), suggesting that *the averaging mechanism of the SF optimizer may mitigate this instability*. Motivated by this observation, we use Muon as the base optimizer under the SF optimizer (we refer to this variant as *SF-Muon*) and analyze the resulting trajectories.

With Muon as the base optimizer, we define the corresponding SF formulation for matrix-valued parameters:

$$\begin{aligned}
 \mathbf{Y}_t &= (1 - \beta)\mathbf{Z}_t + \beta\mathbf{X}_t, \\
 \mathbf{M}_t &= \mu\mathbf{M}_{t-1} + \nabla\mathcal{L}(\mathbf{Y}_t), \\
 \mathbf{Z}_{t+1} &= \mathbf{Z}_t - \eta\mathcal{O}(\mathbf{M}_t), \\
 \mathbf{X}_{t+1} &= (1 - c_{t+1})\mathbf{X}_t + c_{t+1}\mathbf{Z}_{t+1}.
 \end{aligned} \tag{4}$$

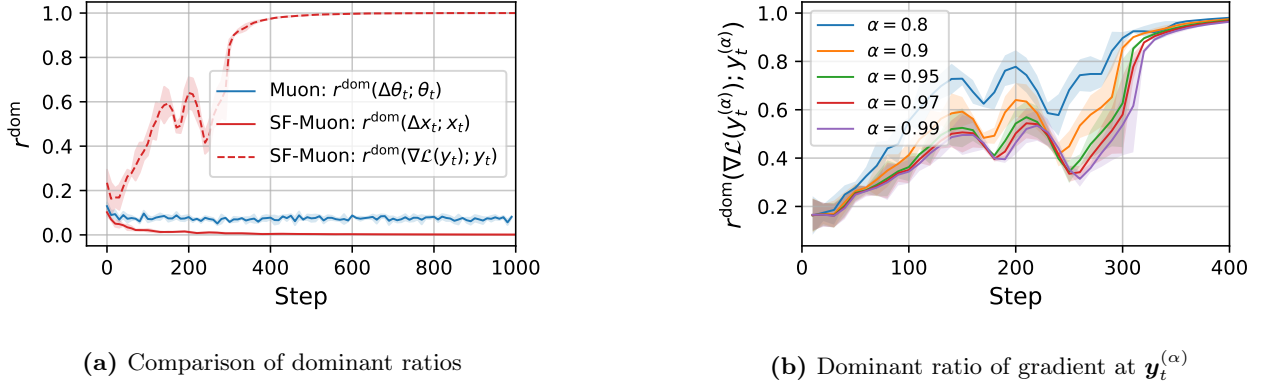


Figure 3: Comparison of dominant component ratios. Settings as in Figure 2. (a) Dominant ratios for Muon (blue) and SF-Muon (red). The solid and dashed red lines denote the dominant components of $\Delta\mathbf{x}_t$ and $\nabla\mathcal{L}(\mathbf{y}_t)$, respectively. (b) Dominant ratios for gradients at $\mathbf{y}_t^{(\alpha)} = (1 - \alpha)\mathbf{z}_t + \alpha\mathbf{x}_t$ across varying α , demonstrating that larger α values correlate with lower dominant components.

Here, \mathbf{Z}_t is the base sequence updated by Muon, \mathbf{Y}_t is the gradient-evaluation point, and \mathbf{X}_t is the averaged sequence used as the final model parameter, with $c_{t+1} = 1/(t + 1)$. The coefficient β determines where the gradient is evaluated between the fast-moving base sequence \mathbf{Z}_t and the averaged sequence \mathbf{X}_t . Although Eq. (4) is written for a single Muon-updated matrix block, not all parameters are updated by Muon. Non-matrix parameters are updated using their corresponding SF base optimizer, such as SF-SGD or SF-AdamW.

To understand how SF interacts with Muon, we measure subspace ratios in the full parameter space. Using the notation of Eq. (1), let $\mathbf{x}_t, \mathbf{y}_t, \mathbf{z}_t \in \mathbb{R}^d$ denote the averaged sequence, gradient-evaluation point, and base sequence, respectively, obtained by flattening and concatenating all trainable parameters. With $\Delta\mathbf{x}_t := \mathbf{x}_{t+1} - \mathbf{x}_t$, we compute $r^{\text{dom}}(\Delta\mathbf{x}_t; \mathbf{x}_t)$ as well as the ratio for the gradient evaluated at \mathbf{y}_t , $r^{\text{dom}}(\nabla\mathcal{L}(\mathbf{y}_t); \mathbf{y}_t)$.

The results in Figure 3a show that the update of \mathbf{x}_t is predominantly bulk-oriented, indicating that the trajectory primarily follows the river direction. In contrast, the gradient evaluated at \mathbf{y}_t still retains a substantial dominant component, which intensifies as training progresses. This suggests that while the averaging mechanism of SF stabilizes the \mathbf{x}_t trajectory, the gradient passed to Muon may still be computed at a noisy valley-wall location. This raises a natural question:

*Can we further reduce the dominant component before orthogonalization
by evaluating gradients at a point closer to the river?*

To test this hypothesis, we use \mathbf{x}_t as a proxy for a point on the river and evaluate gradients at virtual interpolation points $\mathbf{y}_t^{(\alpha)} = (1 - \alpha)\mathbf{z}_t + \alpha\mathbf{x}_t$ for varying $\alpha \in [0, 1]$, while keeping the actual training trajectory fixed by using a fixed β during training (see Figure 4 for an illustration). At each $\mathbf{y}_t^{(\alpha)}$, we compute the gradient and measure its dominant ratio using Eq. (3).

Figure 3b shows that as α increases, the gradient becomes increasingly bulk-oriented. Thus, evaluating closer to \mathbf{x}_t suppresses valley-wall contributions before the Muon orthogonalization step, yielding a more stable update. Consistent with this mechanism, AMUSE—the time-varying SF-Muon variant introduced in Section 4—suppresses dominant components both before and after orthogonalization (Figure 2b). In the language model experiment, we observe a related effect at the trajectory level: increasing β yields larger averaged-sequence updates $\|\Delta\mathbf{x}_t\|$ (Figure 5, right).

One might therefore try to use a large fixed β throughout training, so that gradients are always evaluated close to \mathbf{x}_t . We test this in

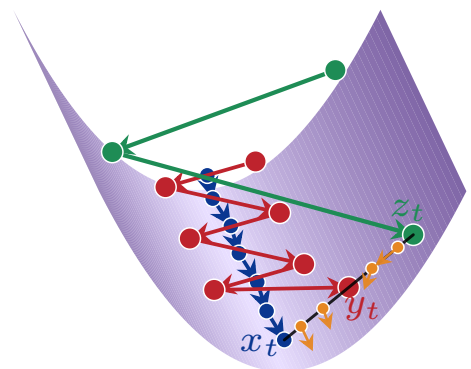


Figure 4: Schedule-free iterates in a river-valley landscape. Orange arrows indicate negative gradients computed at each $\mathbf{y}_t^{(\alpha)}$, exhibiting reduced dominant components when evaluated closer to the river.

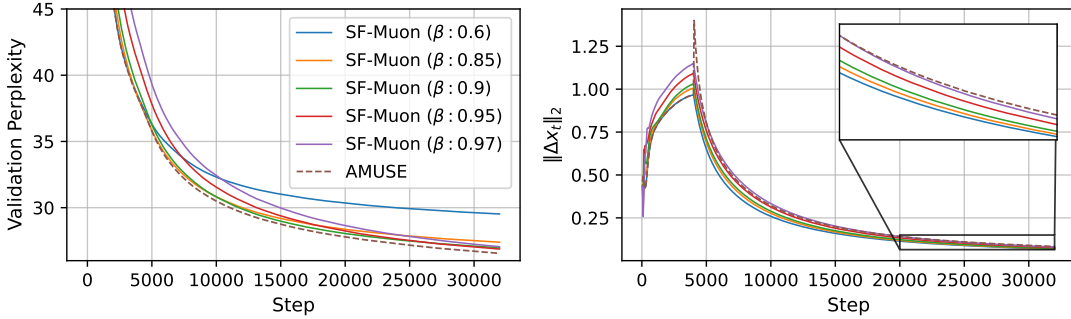


Figure 5: Comparison of fixed- β SF-Muon with different β values and AMUSE in the 124M Llama pretraining on FineWeb. Solid lines show fixed- β SF-Muon, and dashed lines show AMUSE with $\beta_1 = 0.6$ and $\rho = 0.8$. We report validation perplexity (**left**) and the update norm $\|\Delta \mathbf{x}_t\|_2$ (**right**).

the 124M Llama setting with varying β (setup in Section 4), revealing that a large fixed β can be detrimental early in training (Figure 5, left). At this stage, \mathbf{x}_t has not yet reached the river, while \mathbf{z}_t is rapidly approaching it. Consequently, setting a large β evaluates gradients too close to the slower \mathbf{x}_t iterate, causing severe early instability.

4 AMUSE: Anytime MUon with Stable gradient Evaluation

To address the trade-off between early progress and later stability induced by a fixed β , we introduce **Anytime MUon with Stable gradient Evaluation (AMUSE)**. Instead of fixing the interpolation coefficient throughout training, AMUSE employs a time-varying coefficient β_t . It starts with a small β_t to allow fast early adaptation and gradually increases it, shifting the gradient-evaluation point from the fast base trajectory (\mathbf{z}_t) toward the smoother averaged trajectory (\mathbf{x}_t). Formally, AMUSE uses the same update rule as Eq. (4), except the gradient is now evaluated at $\mathbf{Y}_t = (1 - \beta_t)\mathbf{Z}_t + \beta_t\mathbf{X}_t$.

Let T_0 denote the number of warmup steps. During warmup, we fix $\beta_t = \beta_1$. For $t \geq T_0$, we set:

$$\beta_t = 1 - \left(\frac{T_0 - 1}{t - 1} \right)^\rho (1 - \beta_1), \quad (5)$$

where $\rho \in [0, 1]$ controls how quickly β_t increases. When $\rho = 0$, AMUSE reduces to the fixed- β SF-Muon with $\beta_t = \beta_1$; a larger ρ moves the gradient-evaluation point toward \mathbf{x}_t more rapidly. The detailed rationale and derivation for Eq. (5) are deferred to Appendix C.3.

Notably, *this time-varying β_t is independent of the total number of training steps*, gradually approaching 1 as training progresses. Furthermore, like the standard SF method, AMUSE does not require any learning rate schedule. Algorithm 1 in Appendix C.1 summarizes the complete AMUSE procedure.

To verify whether AMUSE behaves as intended, we compare it with fixed- β SF-Muon in Figure 5. We train a 124M Llama model on FineWeb, keeping all hyperparameters fixed except the interpolation coefficient: SF-Muon uses different constant β values, while AMUSE uses the time-varying β_t from Eq. (5). A small fixed β achieves better early performance but degrades late-stage performance, whereas a large fixed β improves performance in the later stages at the cost of higher early perplexity. AMUSE balances these effects by gradually increasing β_t , yielding a Pareto-optimal perplexity curve while maintaining a larger $\|\Delta \mathbf{x}_t\|_2$, which indicates faster progress through the river.

4.1 AMUSE Follows the River

Following Song et al. (2025b), we test whether AMUSE already follows the river using two post-hoc evaluations: Exponential Weight Averaging (EWA) and an additional learning rate decay phase. If the optimizer still oscillates across the valley walls, these procedures should substantially reduce the loss by moving the iterate closer to the river; if it already tracks the river, they should offer little benefit.

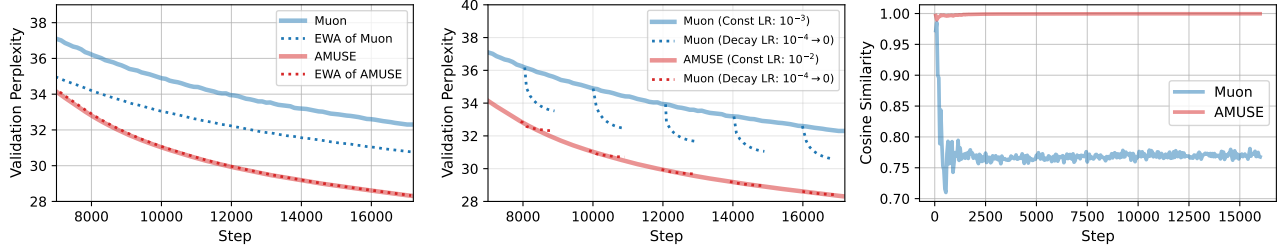


Figure 6: Comparison between constant learning rate Muon and AMUSE in the 124M Llama setting. **The left panel** shows the effect of EWA, where solid lines represent the original training trajectories and dotted lines represent their corresponding EWA trajectories. **The middle panel** shows the effect of learning rate decay, where after warmup we linearly decay the learning rate from 10^{-4} to 0 at selected iterations using the Muon optimizer; solid lines denote the original trajectories, while dotted lines show the corresponding decay-phase trajectories. **The right panel** shows cosine similarity between consecutive updates, plotting $\cos(\Delta \mathbf{x}_t, \Delta \mathbf{x}_{t+1})$ for AMUSE and $\cos(\Delta \theta_t, \Delta \theta_{t+1})$ for Muon.

As shown in Figure 6, constant learning rate Muon benefits significantly from both EWA and learning rate decay, indicating strong valley-wall oscillation. In contrast, AMUSE shows little improvement from either procedure, suggesting it already stays near the river. This stable progress is further confirmed by AMUSE’s high cosine similarity between consecutive updates of \mathbf{x}_t .

5 Experiments

We evaluate AMUSE across a diverse set of benchmarks covering standard image classification, image segmentation, and large language model (LLM) pretraining. For the standard image domain experiments, we primarily follow the setup of Defazio et al. (2024). For LLM pretraining, we follow Semenov et al. (2026) and adopt their Llama-like decoder-only Transformer setup trained on FineWeb-100B (Penedo et al., 2024). In particular, we consider 124M, 720M, and 1B model sizes.

As baselines, we use SGD with momentum and SF-SGD for CIFAR-10, CIFAR-100, SVHN, ImageNet-1k, and ISIC 2018. AdamW and SF-AdamW are used for the remaining tasks. Across all settings, we additionally include Muon as a shared baseline. For SGD, AdamW and Muon, we employ cosine learning rate schedules across all experiments.

5.1 Image Domain Experiments

Experimental Setup. We evaluate AMUSE on image classification benchmarks on diverse datasets and architectures: Wide-ResNet-16-8 on CIFAR-10 (Krizhevsky et al., 2009; Zagoruyko and Komodakis, 2016), DenseNet on CIFAR-100 (Huang et al., 2017), ResNet-3-96 on SVHN (He et al., 2016; Netzer et al., 2011), and ResNet-50 on ImageNet-1k (Russakovsky et al., 2015). We further evaluate two additional settings: U-Net on ISIC 2018 for image segmentation (Codella et al., 2019; Ronneberger et al., 2015), and MAE fine-tuning with a ViT-B/16 on ImageNet (He et al., 2022). For existing baselines, we use the tuned hyperparameters from Defazio et al. (2024) when available. For Muon and AMUSE, whose settings are not provided, we fairly tune the learning rate, weight decay, and optimizer-specific hyperparameters; details are provided in Appendix D.1.

Experimental Results. As illustrated in Figure 7, AMUSE consistently achieves the best performance among the compared optimizers across all evaluated datasets, tasks, and architectures. It demonstrates *superior anytime performance*: while vanilla Muon requires the full training horizon to reach competitive performance, AMUSE exhibits rapid early progress and maintains the highest accuracy throughout training. Notably, AMUSE remains highly effective for MAE fine-tuning even when the checkpoint was pretrained with AdamW. Vanilla Muon struggles in this setting, suggesting that AMUSE may be applied effectively to models pretrained with conventional optimizers.

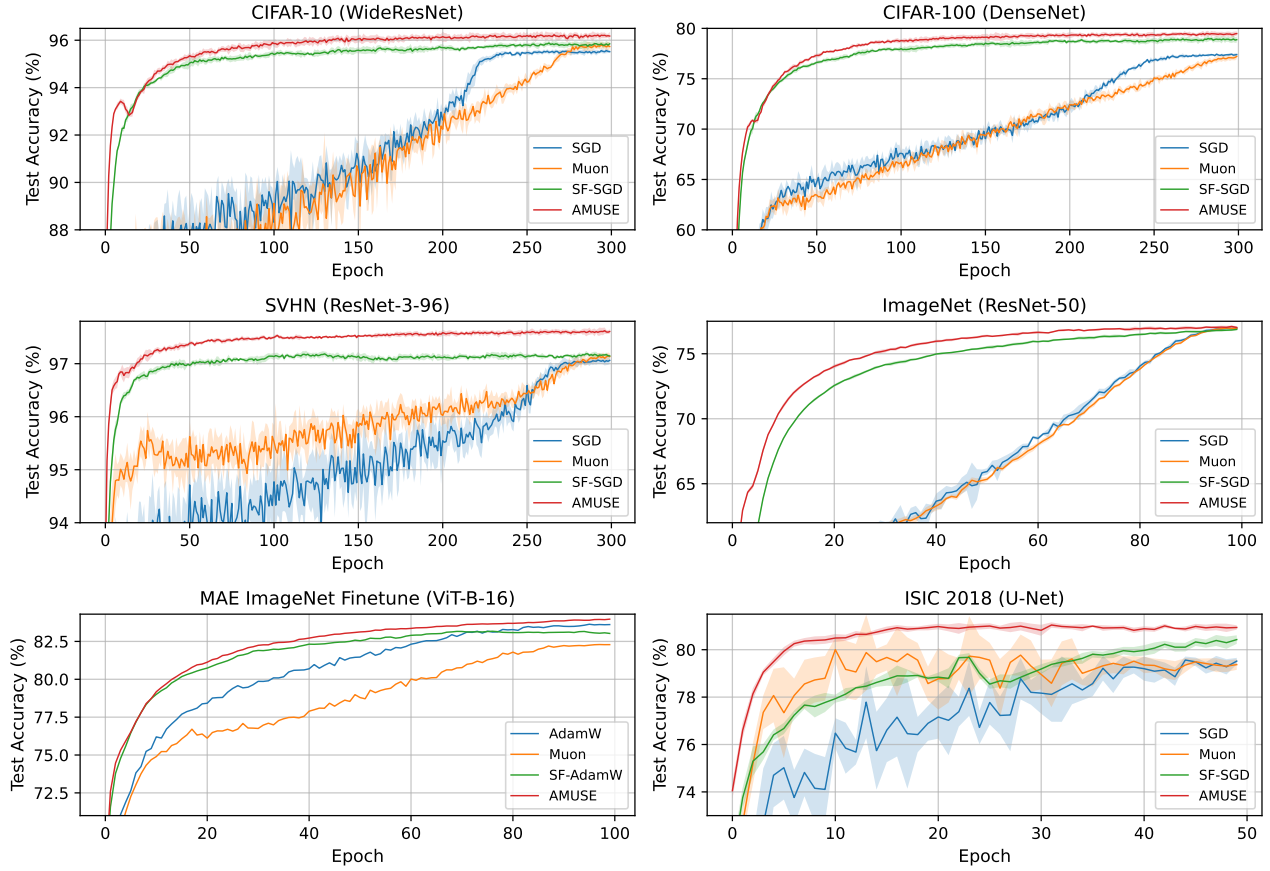


Figure 7: Test accuracy across image domain experiments. Averaged over five random seeds.¹

5.2 Large Language Model Pretraining

Experimental Setup. We follow the Llama-style Transformer setup of [Semenov et al. \(2026\)](#), using tied input/output embeddings, SwiGLU, RMSNorm, and RoPE. We train 124M, 720M, and 1B models on FineWeb-100B ([Penedo et al., 2024](#)) with sequence length 512 and batch sizes 256, 1984, and 2048, respectively. The 124M and 720M models are trained for 16k iterations ($\approx 2.1\text{B}$ and $\approx 16.3\text{B}$ tokens, respectively), while the 1B model is trained for 19.6k iterations ($\approx 20.6\text{B}$ tokens). For baseline optimizers, we use the highly tuned hyperparameters from [Semenov et al. \(2026\)](#), including learning rate, weight decay, scheduler, warmup steps, and momentum. For AMUSE, we tune the corresponding hyperparameters under the same experimental setup, along with $\beta_1 \in \{0.4, 0.6\}$ and $\rho \in \{0.6, 0.8\}$. See Appendix E.2 for more details.

Experimental Results. The results in Figure 8 show that AMUSE consistently improves LLM pretraining. Across all Llama model scales, it achieves lower validation perplexity than all baselines throughout the entire training horizon. Furthermore, extended training results for the 124M model confirm that AMUSE continues to outperform all baselines (Figure 20 in Appendix F.3). We also compare AMUSE with other recent optimizers in Figure 17 (Appendix F.1), demonstrating that it consistently improves the performance-iteration Pareto frontier. Notably, while SF-AdamW struggles with the large batch sizes typically required for modern LLMs ([Morwani et al., 2025](#)), AMUSE scales effectively, maintaining strong performance on the 720M and 1B models trained with large batches.

We further test whether adding exponential weight averaging or a decay phase to constant learning rate Muon recovers AMUSE’s performance. As detailed in Appendix F.2, while these variants improve Muon, they still fall short of AMUSE. This suggests AMUSE inherently maintains a stable trajectory, rather than merely mimicking weight averaging or learning rate decay.

¹MAE fine-tuning is the only exception, reported with a single random seed due to computational constraints.

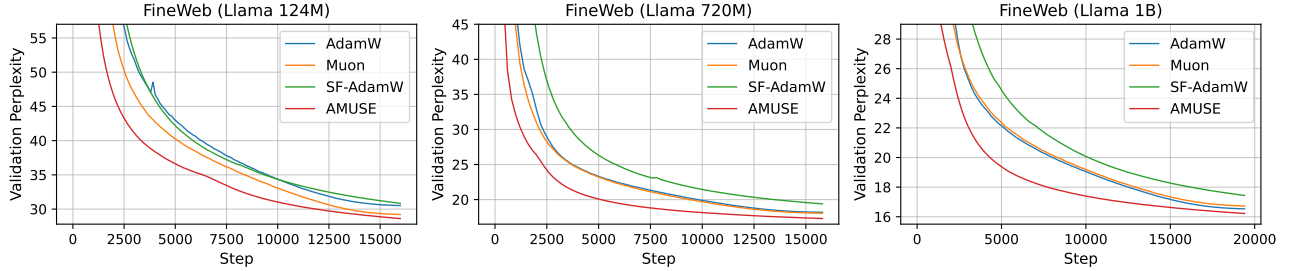


Figure 8: Validation perplexity on FineWeb pretraining across Llama model scales.

5.3 Hyperparameter Sensitivity

In all experiments, we fix the Muon momentum μ and do not treat it as a tunable parameter. Therefore, compared to standard SF optimizers, AMUSE introduces only one additional hyperparameter, ρ , which controls how quickly the gradient evaluation point moves toward the averaged iterate. We evaluate the hyperparameter sensitivity of AMUSE to ρ and β_1 on Llama 124M (see Appendix F.4).

5.4 Implementation Details

For language model pretraining and MAE fine-tuning, we optimize non-Muon parameters, such as embeddings, normalization layers, and output heads, with SF-AdamW; for other image-domain experiments, we use SF-SGD, following standard Muon practice.

Although AMUSE is formulated with three sequences $(\mathbf{x}_t, \mathbf{y}_t, \mathbf{z}_t)$ from the standard SF formulation and a muon momentum buffer \mathbf{m}_t , its practical implementation requires storing only the model parameters (kept at \mathbf{y}_t), the sequence state \mathbf{z}_t , and the momentum buffer \mathbf{m}_t . For evaluation, we temporarily compute \mathbf{x}_t via in-place interpolation using \mathbf{y}_t and \mathbf{z}_t , and revert the parameters afterward. Because of this design, AMUSE requires exactly one extra state copy (\mathbf{z}_t) compared to vanilla Muon, *incurring no additional memory overhead compared to AdamW and SF-AdamW*. While AMUSE still utilizes a standard linear warmup phase, $\eta_t = \eta \min(1, t/T_0)$, it does not require a subsequent learning rate decay phase. For other implementation details, see Appendix C.4.

6 Conclusion

We introduce AMUSE, an optimization algorithm designed to stabilize Muon using the SF framework and a time-varying interpolation parameter β_t . We observe that Muon’s orthogonalization operator promotes training by leveraging large bulk components, but also induces oscillations along valley walls, thereby contributing to its inherent instability. AMUSE adopts the SF framework, a principled approach that controls where the gradient is evaluated and stabilizes training by keeping the optimization trajectory close to the river geometry. With a carefully designed schedule for the interpolation parameter β_t , AMUSE outperforms conventional learning-rate-scheduled Adam(W) or Muon optimizers across a wide range of deep learning tasks. Our results highlight how a systematic understanding of training dynamics and the loss landscape provides a principled approach to optimizer design.

Despite the superior performance of AMUSE compared with various optimizers including Muon, it requires additional memory overhead relative to vanilla Muon. Developing an optimization strategy that enhances updates along the river direction and suppresses valley-wall oscillations without incurring such overhead is a promising direction for future investigation.

References

Sanjeev Arora, Zhiyuan Li, and Abhishek Panigrahi. Understanding gradient descent on the edge of stability in deep learning. In *International Conference on Machine Learning*, pages 948–1024. PMLR, 2022.

- Annalisa Belloni, Lorenzo Noci, and Antonio Orvieto. Universal dynamics of warmup stable decay: understanding WSD beyond transformers. In *High-dimensional Learning Dynamics 2025*, 2025. URL <https://openreview.net/forum?id=QJfH01BZ8d>.
- Jeremy Bernstein and Laker Newhouse. Old optimizer, new norm: An anthology. In *OPT 2024: Optimization for Machine Learning*, 2024. URL <https://openreview.net/forum?id=ux18f5n0pD>.
- Noel Codella, Veronica Rotemberg, Philipp Tschandl, M Emre Celebi, Stephen Dusza, David Gutman, Brian Helba, Aadi Kaloo, Konstantinos Liopyris, Michael Marchetti, et al. Skin lesion analysis toward melanoma detection 2018: A challenge hosted by the international skin imaging collaboration (isic). *arXiv preprint arXiv:1902.03368*, 2019.
- Jeremy Cohen, Simran Kaur, Yuanzhi Li, J Zico Kolter, and Ameet Talwalkar. Gradient descent on neural networks typically occurs at the edge of stability. In *International Conference on Learning Representations*, 2021. URL <https://openreview.net/forum?id=jh-rTtvkGeM>.
- Jeremy Cohen, Alex Damian, Ameet Talwalkar, J Zico Kolter, and Jason D. Lee. Understanding optimization in deep learning with central flows. In *The Thirteenth International Conference on Learning Representations*, 2025. URL <https://openreview.net/forum?id=sIE2rI3ZPs>.
- George E Dahl, Frank Schneider, Zachary Nado, Naman Agarwal, Chandramouli Shama Sastry, Philipp Hennig, Sourabh Medapati, Runa Eschenhagen, Priya Kasimbeg, Daniel Suo, et al. Benchmarking neural network training algorithms. *arXiv preprint arXiv:2306.07179*, 2023.
- Alex Damian, Eshaan Nichani, and Jason D Lee. Self-stabilization: The implicit bias of gradient descent at the edge of stability. *arXiv preprint arXiv:2209.15594*, 2022.
- DeepSeek-AI. DeepSeek-V4: Towards highly efficient million-token context intelligence, 2026.
- Aaron Defazio, Xingyu Alice Yang, Ahmed Khaled, Konstantin Mishchenko, Harsh Mehta, and Ashok Cutkosky. The road less scheduled. In *The Thirty-eighth Annual Conference on Neural Information Processing Systems*, 2024. URL <https://openreview.net/forum?id=0XeNkkENuI>.
- Shenyang Deng, Boyao Liao, Zhuoli Ouyang, Tianyu Pang, Minhak Song, and Yaoqing Yang. Suspicious alignment of SGD: a fine-grained step size condition analysis. In *Proceedings of The 37th International Conference on Algorithmic Learning Theory*, volume 313 of *Proceedings of Machine Learning Research*, pages 1–66, 2026.
- Behrooz Ghorbani, Shankar Krishnan, and Ying Xiao. An investigation into neural net optimization via hessian eigenvalue density. In *International Conference on Machine Learning*, pages 2232–2241. PMLR, 2019.
- GLM-5 Team. GLM-5: from vibe coding to agentic engineering. *arXiv preprint arXiv:2602.15763*, 2026.
- Kaiming He, Xiangyu Zhang, Shaoqing Ren, and Jian Sun. Deep residual learning for image recognition. In *Proceedings of the IEEE Conference on Computer Vision and Pattern Recognition (CVPR)*, June 2016.
- Kaiming He, Xinlei Chen, Saining Xie, Yanghao Li, Piotr Dollár, and Ross Girshick. Masked autoencoders are scalable vision learners. In *Proceedings of the IEEE/CVF conference on computer vision and pattern recognition*, pages 16000–16009, 2022.
- Wei He, Kai Han, Hang Zhou, Hanting Chen, Zhicheng Liu, Xinghao Chen, and Yunhe Wang. Root: Robust orthogonalized optimizer for neural network training. *arXiv preprint arXiv:2511.20626*, 2025.
- Gao Huang, Zhuang Liu, Laurens van der Maaten, and Kilian Q. Weinberger. Densely connected convolutional networks. In *Proceedings of the IEEE Conference on Computer Vision and Pattern Recognition (CVPR)*, July 2017.
- Keller Jordan, Yuchen Jin, Vlado Boza, Jiacheng You, Franz Cesista, Laker Newhouse, and Jeremy Bernstein. Muon: An optimizer for hidden layers in neural networks, 2024. URL <https://kellerjordan.github.io/posts/muon/>.
- Changmin Kang, Jihun Yun, Baekrok Shin, Yeseul Cho, and Chulhee Yun. Uniform spectral growth and convergence of muon in lora-style matrix factorization. *arXiv preprint arXiv:2602.06385*, 2026.

- Priya Kasimbeg, Frank Schneider, Runa Eschenhagen, Juhan Bae, Chandramouli Shama Sastry, Mark Saroufim, BOYUAN FENG, Less Wright, Edward Z. Yang, Zachary Nado, Sourabh Medapati, Philipp Hennig, Michael Rabbat, and George E. Dahl. Accelerating neural network training: An analysis of the algoperf competition. In *The Thirteenth International Conference on Learning Representations*, 2025. URL <https://openreview.net/forum?id=CtM5xjRSfm>.
- Kimi Team. Kimi K2: Open agentic intelligence. *arXiv preprint arXiv:2507.20534*, 2025.
- Diederik P. Kingma and Jimmy Ba. Adam: A method for stochastic optimization. In *3rd International Conference on Learning Representations*, 2015.
- Alex Krizhevsky, Geoffrey Hinton, et al. Learning multiple layers of features from tiny images. 2009.
- Jingyuan Liu, Jianlin Su, Xingcheng Yao, Zhejun Jiang, Guokun Lai, Yulun Du, Yidao Qin, Weixin Xu, Enzhe Lu, Junjie Yan, et al. Muon is scalable for LLM training. *arXiv preprint arXiv:2502.16982*, 2025a.
- Yizhou Liu, Ziming Liu, and Jeff Gore. Focus: First order concentrated updating scheme. *arXiv preprint arXiv:2501.12243*, 2025b.
- Ilya Loshchilov and Frank Hutter. SGDR: Stochastic gradient descent with warm restarts. In *International Conference on Learning Representations*, 2017. URL <https://openreview.net/forum?id=Skq89Scxx>.
- Ilya Loshchilov and Frank Hutter. Decoupled weight decay regularization. In *International Conference on Learning Representations*, 2019.
- Kairong Luo, Zhenbo Sun, Haodong Wen, Xinyu Shi, Jiarui Cui, Chenyi Dang, Kaifeng Lyu, and Wenguang Chen. How learning rate decay wastes your best data in curriculum-based LLM pretraining. In *The Fourteenth International Conference on Learning Representations*, 2026. URL <https://openreview.net/forum?id=T5wkZJqzkz>.
- Jianhao Ma, Yu Huang, Yuejie Chi, and Yuxin Chen. Preconditioning benefits of spectral orthogonalization in muon. *arXiv preprint arXiv:2601.13474*, 2026.
- Deven Morwani, Nikhil Vyas, Hanlin Zhang, and Sham Kakade. Connections between schedule-free optimizers, ademamix, and accelerated sgd variants. *arXiv preprint arXiv:2502.02431*, 2025.
- Yurii Nesterov. Primal-dual subgradient methods for convex problems. *Mathematical programming*, 120(1): 221–259, 2009.
- Yuval Netzer, Tao Wang, Adam Coates, Alessandro Bissacco, Baolin Wu, Andrew Y Ng, et al. Reading digits in natural images with unsupervised feature learning. In *NIPS workshop on deep learning and unsupervised feature learning*, volume 2011, page 4. Granada, 2011.
- Vardan Papyan. The full spectrum of deepnet Hessians at scale: Dynamics with sgd training and sample size. *arXiv preprint arXiv:1811.07062*, 2018.
- Vardan Papyan. Measurements of three-level hierarchical structure in the outliers in the spectrum of deepnet Hessians. In *International Conference on Machine Learning*, pages 5012–5021. PMLR, 2019.
- Vardan Papyan. Traces of class/cross-class structure pervade deep learning spectra. *Journal of Machine Learning Research*, 21(252):1–64, 2020. URL <http://jmlr.org/papers/v21/20-933.html>.
- Guilherme Penedo, Hynek Kydlíček, Loubna Ben allal, Anton Lozhkov, Margaret Mitchell, Colin Raffel, Leandro Von Werra, and Thomas Wolf. The fineweb datasets: Decanting the web for the finest text data at scale. In *The Thirty-eight Conference on Neural Information Processing Systems Datasets and Benchmarks Track*, 2024. URL <https://openreview.net/forum?id=n6SCKn2QaG>.
- Boris T Polyak and Anatoli B Juditsky. Acceleration of stochastic approximation by averaging. *SIAM journal on control and optimization*, 30(4):838–855, 1992.
- Xianbiao Qi, Marco Chen, Jiaquan Ye, Yelin He, and Rong Xiao. Delving into muon and beyond: Deep analysis and extensions. *arXiv preprint arXiv:2602.04669*, 2026.

- Olaf Ronneberger, Philipp Fischer, and Thomas Brox. U-net: Convolutional networks for biomedical image segmentation. In *International Conference on Medical image computing and computer-assisted intervention*, pages 234–241. Springer, 2015.
- David Ruppert. Efficient estimations from a slowly convergent robbins-monro process. Technical report, Cornell University Operations Research and Industrial Engineering, 1988.
- Olga Russakovsky, Jia Deng, Hao Su, Jonathan Krause, Sanjeev Satheesh, Sean Ma, Zhiheng Huang, Andrej Karpathy, Aditya Khosla, Michael Bernstein, et al. Imagenet large scale visual recognition challenge. *International journal of computer vision*, 115(3):211–252, 2015.
- Levent Sagun, Leon Bottou, and Yann LeCun. Eigenvalues of the hessian in deep learning: Singularity and beyond. *arXiv preprint arXiv:1611.07476*, 2016.
- Levent Sagun, Utku Evci, V Ugur Guney, Yann Dauphin, and Leon Bottou. Empirical analysis of the hessian of over-parametrized neural networks. *arXiv preprint arXiv:1706.04454*, 2017.
- Andrei Semenov, Matteo Pagliardini, and Martin Jaggi. Benchmarking optimizers for large language model pretraining, 2026. URL <https://openreview.net/forum?id=Jw7khYzYz1>.
- Wei Shen, Ruichuan Huang, Minhui Huang, Cong Shen, and Jiawei Zhang. On the convergence analysis of muon. *arXiv preprint arXiv:2505.23737*, 2025.
- Minhak Song, Kwangjun Ahn, and Chulhee Yun. Does SGD really happen in tiny subspaces? In *The Thirteenth International Conference on Learning Representations*, 2025a. URL <https://openreview.net/forum?id=v6iLQBoIJw>.
- Minhak Song, Beomhan Baek, Kwangjun Ahn, and Chulhee Yun. Through the river: Understanding the benefit of schedule-free methods for language model training. In *The Thirty-ninth Annual Conference on Neural Information Processing Systems*, 2025b. URL <https://openreview.net/forum?id=CGx4XU9rCA>.
- Wei Tao, Zhisong Pan, Gaowei Wu, and Qing Tao. Primal averaging: A new gradient evaluation step to attain the optimal individual convergence. *IEEE transactions on cybernetics*, 50(2):835–845, 2018.
- Bhavya Vasudeva, Puneesh Deora, Yize Zhao, Vatsal Sharan, and Christos Thrampoulidis. How muon’s spectral design benefits generalization: A study on imbalanced data. In *The Fourteenth International Conference on Learning Representations*, 2026. URL <https://openreview.net/forum?id=YzjS4jcfmS>.
- Jinbo Wang, Mingze Wang, Zhanpeng Zhou, Junchi Yan, Weinan E, and Lei Wu. The sharpness disparity principle in transformers for accelerating language model pre-training. In *Forty-second International Conference on Machine Learning*, 2025. URL <https://openreview.net/forum?id=DZ6iFdVDrx>.
- Mingze Wang, Jinbo Wang, Haotian He, Zilin Wang, Guanhua Huang, Feiyu Xiong, Zhiyu li, Weinan E, and Lei Wu. Improving generalization and convergence by enhancing implicit regularization. In *The Thirty-eighth Annual Conference on Neural Information Processing Systems*, 2024. URL <https://openreview.net/forum?id=cjM2bhL0iC>.
- Kaiyue Wen, Zhiyuan Li, Jason S. Wang, David Leo Wright Hall, Percy Liang, and Tengyu Ma. Understanding warmup-stable-decay learning rates: A river valley loss landscape view. In *The Thirteenth International Conference on Learning Representations*, 2025. URL <https://openreview.net/forum?id=m51BgoqvBP>.
- Yuxin Wu and Justin Johnson. Rethinking “batch” in batchnorm. *arXiv preprint arXiv:2105.07576*, 2021.
- Zhewei Yao, Amir Gholami, Kurt Keutzer, and Michael W Mahoney. Pyhessian: Neural networks through the lens of the hessian. In *2020 IEEE international conference on big data (Big data)*, pages 581–590. IEEE, 2020.
- Sergey Zagoruyko and Nikos Komodakis. Wide residual networks. *CoRR*, abs/1605.07146, 2016. URL <http://arxiv.org/abs/1605.07146>.
- Minxin Zhang, Yuxuan Liu, and Hayden Schaeffer. Adam improves muon: Adaptive moment estimation with orthogonalized momentum. *arXiv preprint arXiv:2602.17080*, 2026a.

Yechen Zhang, Shuhao Xing, Junhao Huang, Kai Lv, Yunhua Zhou, Xipeng Qiu, Qipeng Guo, and Kai Chen. Mousse: Rectifying the geometry of muon with curvature-aware preconditioning. *arXiv preprint arXiv:2603.09697*, 2026b.

Wenjie Zhou, Bohan Wang, Wei Chen, and Xueqi Cheng. Bsfa: Leveraging the subspace dichotomy to accelerate neural network training. In *Proceedings of the 2025 Conference on Empirical Methods in Natural Language Processing*, pages 18845–18860, 2025.

Shuchen Zhu, Rizhen Hu, Mingze Wang, Mou Sun, Xue Wang, Kun Yuan, and Zaiwen Wen. Accelerating llm pre-training through flat-direction dynamics enhancement. *arXiv preprint arXiv:2602.22681*, 2026.

Contents

1	Introduction	1
2	Related Work	3
2.1	River-Valley Loss Landscape	3
2.2	Schedule-Free Optimizer	3
2.3	Muon Optimizer	3
3	A River-Valley Analysis of Muon and Schedule-Free Dynamics	4
3.1	Orthogonalization Makes Muon Updates More Bulk-Oriented	5
3.2	Schedule-Free Stabilizes Muon Trajectories	5
4	AMUSE: Anytime MUon with Stable gradient Evaluation	7
4.1	AMUSE Follows the River	7
5	Experiments	8
5.1	Image Domain Experiments	8
5.2	Large Language Model Pretraining	9
5.3	Hyperparameter Sensitivity	10
5.4	Implementation Details	10
6	Conclusion	10
A	A Quadratic Example of Bouncing in Matrix-Normalized Updates	16
B	Additional Results and Experimental Details for Section 3	18
B.1	Dominant Updates Can Cause Instability, while Bulk Updates Accelerate Training	18
B.2	Experimental Details	19
B.3	Additional Experimental Results	20
C	Details for AMUSE	24
C.1	Algorithmic Description of AMUSE	24
C.2	Averaging Orthogonalized Updates	25
C.3	Derivation of the β_t Schedule	26
C.4	Implementation Details	28
D	Image Domain Experiments	29
D.1	Experimental Details	29
E	Large Language Model Experiments	33
E.1	Architecture Details	33
E.2	Hyperparameter Tuning	33
F	Additional Experiments	36
F.1	Comparison with Additional Optimizer Baselines	36
F.2	Comparison with Muon with EWA and WSD	36
F.3	Longer Training Result	37
F.4	Hyperparameter Sensitivity	38
F.5	Wall-clock Time Comparison	39
F.6	Ablation Studies	39

A A Quadratic Example of Bouncing in Matrix-Normalized Updates

We compare standard gradient descent (GD) with an idealized matrix-normalized update on a two-dimensional matrix quadratic objective. This example is not intended to model the full momentum dynamics of Muon, but rather isolates the magnitude-removing effect of polar normalization. We use an anisotropic setting to show that matrix normalization removes gradient magnitude information, which can cause bouncing of small nonzero components near the optimum.

Let $\mathbf{W} \in \mathbb{R}^{2 \times 2}$ be the parameter matrix, and let $\mathbf{A} \in \mathbb{R}^{2 \times 2}$ be a symmetric positive definite matrix with an anisotropic spectrum:

$$\mathbf{A} = \mathbf{Q}\mathbf{\Lambda}\mathbf{Q}^\top, \quad \mathbf{\Lambda} = \begin{pmatrix} \lambda & 0 \\ 0 & 1 \end{pmatrix},$$

where \mathbf{Q} is an orthogonal matrix, and $\lambda \gg 1$ controls the curvature gap between the first and second principal directions. We consider the quadratic objective

$$f(\mathbf{W}) = \frac{1}{2} \text{tr}(\mathbf{W}^\top \mathbf{A} \mathbf{W}),$$

where the gradient is $\nabla f(\mathbf{W}) = \mathbf{A}\mathbf{W}$. To analyze the dynamics, we project the parameters into the eigenbasis of \mathbf{A} by defining $\mathbf{V}_t = \mathbf{Q}^\top \mathbf{W}_t$. Consider a diagonal iterate in this eigenbasis:

$$\mathbf{V}_t = \begin{pmatrix} a_t & 0 \\ 0 & b_t \end{pmatrix}.$$

Then, $\mathbf{W}_t = \mathbf{Q}\mathbf{V}_t$, and the gradient is:

$$\nabla f(\mathbf{W}_t) = \mathbf{A}\mathbf{W}_t = (\mathbf{Q}\mathbf{\Lambda}\mathbf{Q}^\top)(\mathbf{Q}\mathbf{V}_t) = \mathbf{Q}\mathbf{\Lambda}\mathbf{V}_t = \mathbf{Q} \begin{pmatrix} \lambda a_t & 0 \\ 0 & b_t \end{pmatrix}.$$

Gradient Descent Dynamics. GD with step size η gives $\mathbf{W}_{t+1}^{\text{GD}} = \mathbf{W}_t - \eta \nabla f(\mathbf{W}_t)$. Projecting this update into the eigenbasis yields:

$$\mathbf{V}_{t+1}^{\text{GD}} = \mathbf{V}_t - \eta \mathbf{\Lambda} \mathbf{V}_t.$$

For the first coordinate, we have $a_{t+1}^{\text{GD}} = (1 - \eta\lambda)a_t$.

If $0 < \eta < 1/\lambda$, then $0 < 1 - \eta\lambda < 1$, so

$$|a_{t+1}^{\text{GD}}| < |a_t|, \quad \text{sign}(a_{t+1}^{\text{GD}}) = \text{sign}(a_t).$$

The update magnitude in the first coordinate is $|\Delta a_t^{\text{GD}}| = \eta\lambda|a_t|$, which goes to zero as $a_t \rightarrow 0$.

Matrix-Normalized Dynamics. Now consider a matrix-normalized update, which idealizes the normalization effect of Muon. For a full-rank matrix \mathbf{G} , define its polar factor as:

$$\text{Polar}(\mathbf{G}) = \mathbf{G}(\mathbf{G}^\top \mathbf{G})^{-1/2}.$$

We apply this to the gradient $\mathbf{G}_t = \nabla f(\mathbf{W}_t) = \mathbf{Q}\mathbf{\Lambda}\mathbf{V}_t$. When $a_t \neq 0$ and $b_t \neq 0$, we have:

$$\mathbf{G}_t^\top \mathbf{G}_t = \mathbf{V}_t^\top \mathbf{\Lambda}^\top \mathbf{Q}^\top \mathbf{Q} \mathbf{\Lambda} \mathbf{V}_t = \begin{pmatrix} (\lambda a_t)^2 & 0 \\ 0 & b_t^2 \end{pmatrix}.$$

The inverse square root is $\text{diag}(|\lambda a_t|^{-1}, |b_t|^{-1})$. Therefore,

$$\text{Polar}(\mathbf{G}_t) = \mathbf{Q} \begin{pmatrix} \lambda a_t & 0 \\ 0 & b_t \end{pmatrix} \begin{pmatrix} |\lambda a_t|^{-1} & 0 \\ 0 & |b_t|^{-1} \end{pmatrix} = \mathbf{Q} \begin{pmatrix} \text{sign}(a_t) & 0 \\ 0 & \text{sign}(b_t) \end{pmatrix}.$$

The matrix-normalized update is $\mathbf{W}_{t+1}^{\text{MN}} = \mathbf{W}_t - \eta \text{Polar}(\nabla f(\mathbf{W}_t))$. Projecting this back into the eigenbasis ($\mathbf{V}_{t+1}^{\text{MN}} = \mathbf{Q}^\top \mathbf{W}_{t+1}^{\text{MN}}$) gives $a_{t+1}^{\text{MN}} = a_t - \eta \text{sign}(a_t)$.

The contrast is therefore clear. GD preserves the magnitude information of the gradient, while the matrix-normalized update removes it through polar decomposition. For every nonzero a_t in this full-rank regime, the matrix-normalized step magnitude remains constant:

$$|\Delta a_t^{\text{MN}}| = \eta.$$

If $0 < |a_t| < \eta$, then

$$a_t a_{t+1}^{\text{MN}} < 0,$$

so the first coordinate changes sign in one step. Moreover, if $0 < a_t < \eta$, then

$$a_{t+2}^{\text{MN}} = a_t,$$

so the dynamics forms a two-cycle along this coordinate. Thus, unlike GD, the matrix-normalized update does not shrink as the component becomes arbitrarily small but nonzero. A small residual component can therefore receive a constant update and bounce across zero.

B Additional Results and Experimental Details for Section 3

In this section we provide additional experimental details and results for the analysis in Section 3. We include experimental setups and additional results that were omitted from the main text due to space constraints.

B.1 Dominant Updates Can Cause Instability, while Bulk Updates Accelerate Training

In this subsection, we empirically show that updates along the dominant directions can cause training instability, while amplifying the bulk component can accelerate Muon training. Following Zhou et al. (2025), we do this by decomposing each Muon update into its dominant and bulk components and scaling them separately.

We conduct experiments on three classification datasets: MNIST, CIFAR-10, and SST-2. Detailed experimental settings, including dataset construction and model architectures, are provided in Section B.2; hyperparameters are reported in the corresponding figure captions.

We use the dominant and bulk subspaces defined in Definition 3.1. That is, for the Hessian $\nabla^2\mathcal{L}(\theta_t)$, the dominant subspace $\mathcal{S}_k(\theta_t)$ is spanned by the top- k eigenvectors, and the bulk subspace is its orthogonal complement $\mathcal{S}_k^\perp(\theta_t)$. Following the observation that the Hessian spectrum of classification models contains a small number of outlier eigenvalues related to the number of classes, we set k to the number of classes: $k = 10$ for MNIST-5k and CIFAR-10-5k, and $k = 2$ for SST-2-1k.

Let \mathbf{M}_t denote the matrix-valued Muon momentum and define the flattened post-orthogonalized update direction as $\mathbf{u}_t = \text{vec}(\mathcal{O}(\mathbf{M}_t))$. Using the subspace projection matrices from Definition 3.2, we decompose \mathbf{u}_t into dominant and bulk components as $\mathbf{P}_k(\theta_t)\mathbf{u}_t$ and $\mathbf{P}_k^\perp(\theta_t)\mathbf{u}_t$, respectively. We then rescale the two components separately:

$$\tilde{\mathbf{u}}_t = \alpha\mathbf{P}_k(\theta_t)\mathbf{u}_t + \gamma\mathbf{P}_k^\perp(\theta_t)\mathbf{u}_t,$$

where α and γ are multiplicative scaling factors for the dominant and bulk components, respectively. For example, when $\alpha = \gamma = 1$, this recovers the original Muon update. The parameter is updated by

$$\theta_{t+1} = \theta_t - \eta\tilde{\mathbf{u}}_t.$$

As shown in Figure 9, larger α leads to more unstable training, indicating that dominant-subspace components can induce valley-wall oscillations. In contrast, larger γ improves training speed and leads to more stable convergence, suggesting that bulk directions are responsible for useful optimization progress. These results suggest that reducing dominant components before orthogonalization is important for training stability, while preserving Muon’s strong bulk-oriented updates is important for fast training.

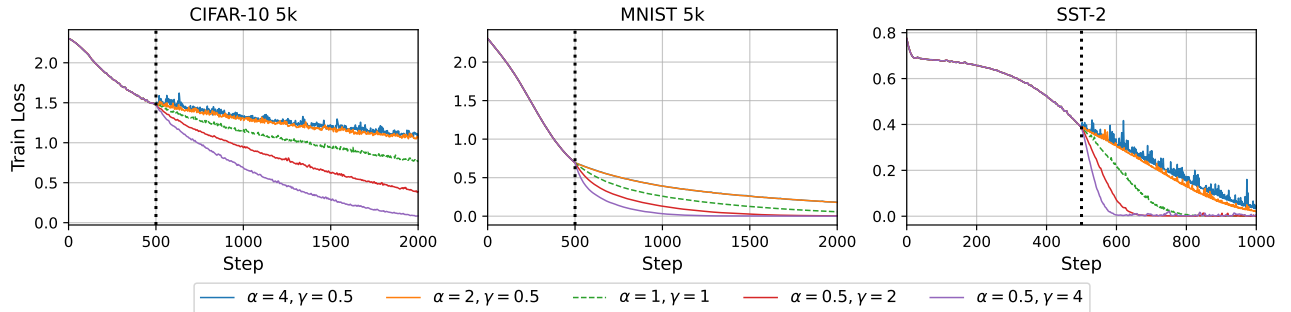


Figure 9: Scaling Dominant (α) and Bulk (γ) components of Muon update. We apply subspace-wise scaling to Muon updates starting at step 500. For CIFAR-10-5k and MNIST-5k, Muon is combined with SGD for non-Muon parameters, using momentum 0.9 and learning rate 5×10^{-4} . For SST-2-1k, Muon is combined with AdamW for non-Muon parameters, using Muon momentum 0.9, AdamW coefficients (0.9, 0.99), and learning rate 1×10^{-4} .

B.2 Experimental Details

We follow the experimental setup of [Cohen et al. \(2021\)](#); [Song et al. \(2025a\)](#) for all experiments in Appendix B.3. For experiments in Appendix B.1, we use the same experimental setup except for introducing scaling factors following [Zhou et al. \(2025\)](#).

B.2.1 Architecture Details

We consider three model architectures, chosen according to the input modality. For fully connected image classification, we use a three-layer MLP with width 200 and Tanh activations, following [Cohen et al. \(2021\)](#); [Song et al. \(2025a\)](#). For convolutional image classification, we use a three-layer CNN with width 32 and ReLU activations, following [Cohen et al. \(2021\)](#); [Song et al. \(2025a\)](#). For text classification, we use a two-layer Transformer with hidden dimension 64 and 8 attention heads, following [Damian et al. \(2022\)](#); [Song et al. \(2025a\)](#).

B.2.2 Datasets

We use three small-scale classification benchmarks constructed from MNIST, CIFAR-10, and SST-2. For MNIST and CIFAR-10, we use the first 5,000 training examples, each with 10 classes. For SST-2, we use the first 1,000 examples for binary sentiment classification. The main text reports the MNIST-5k experiment with MLP architecture in Section 3.

B.2.3 Experimental Setup

In all experiments in this section, including those in Section 3, we use cross-entropy loss with batch size 50. We use a constant learning rate for all optimizers: SGD, AdamW, Muon, and SF-Muon. For Muon and SF-Muon, non-hidden matrix layers are optimized with SGD in the CIFAR-10-5k and MNIST-5k experiments, and with AdamW (and its SF variant in SF-Muon) in the SST-2-1k experiment.

The hyperparameters for each experiment are reported in Tables 2, 1, and 3. Unless otherwise specified, each figure uses the hyperparameters corresponding to its dataset.

For figures requiring additional hyperparameters, we use the following settings:

- Figure 2, Figure 3, and Figure 10: MNIST hyperparameters in Table 1.
- Figure 2b: AMUSE with learning rate 0.01, $\beta_1 = 0.8$, and $\rho = 0.6$.
- Figure 10, Figure 11, and Figure 13: CIFAR-10 hyperparameters in Table 2.
- Figure 10, Figure 11, and Figure 14: SST-2 hyperparameters in Table 3.

Table 1: Hyperparameters for MNIST-5k Experiments.

Optimizer	Learning rate	Momentum
SGD	1e-2	–
AdamW	5e-4	(0.9,0.99)
Muon	1e-3	0.9
SF-Muon ($\beta = 0.9$)	2e-3	0.95

Table 2: Hyperparameters for CIFAR10-5k Experiments.

Optimizer	Learning rate	Momentum
SGD	1e-2	–
AdamW	5e-4	(0.9,0.99)
Muon	2e-3	0.9
SF-Muon ($\beta = 0.8$)	2e-3	0.9

Table 3: Hyperparameters for SST2-1k Experiments.

Optimizer	Learning rate	AdamW Momentum	Muon momentum
AdamW	5e-4	(0.9,0.99)	–
Muon	2e-3	(0.9,0.99)	0.9
SF-Muon ($\beta = 0.8$)	1e-5	(-,0.99)	0.9

B.3 Additional Experimental Results

In this section, we provide additional results for the analysis in Section 3. We organize the results into three parts: Hessian eigenspectra, Muon bulk-ratio behavior, and SF-Muon dynamics.

Hessian eigenspectrum. We first examine the loss Hessian eigenspectrum across datasets and architectures. Figure 10 shows that the Hessian spectrum consistently contains a small number of large outlier eigenvalues, while the remaining eigenvalues are much smaller. This separation supports the dominant/bulk decomposition used in the main text.

Bulk-oriented updates of Muon. We next verify that the bulk-oriented behavior of Muon extends beyond the main setting. Figures 11 and 12 show that Muon produces substantially larger bulk-ratio updates than SGD or AdamW across CIFAR-10 with a CNN and SST-2 with a Transformer. The same figures also compare the pre- and post-orthogonalized Muon updates, showing that the orthogonalization step itself increases the bulk component of the update. These results reinforce the explanation that Muon accelerates training by promoting movement in bulk directions, as mentioned in Section 3.1.

Schedule-Free Muon dynamics. Finally, we repeat the SF-Muon analysis from the main text (Figure 3) on additional settings. Figures 13 and 14 compare the dominant/bulk components of Muon and SF-Muon, and also gradients at multiple virtual interpolation points $\mathbf{y}_t^{(\alpha)} = (1 - \alpha)\mathbf{z}_t + \alpha\mathbf{x}_t$. In both settings, the averaged SF-Muon trajectory has a much smaller dominant component than vanilla Muon, and gradients evaluated closer to \mathbf{x}_t become more bulk-oriented. These results further support the claim that evaluating gradients near the averaged iterate can suppress valley-wall contributions before the Muon orthogonalization step, as mentioned in Section 3.2.

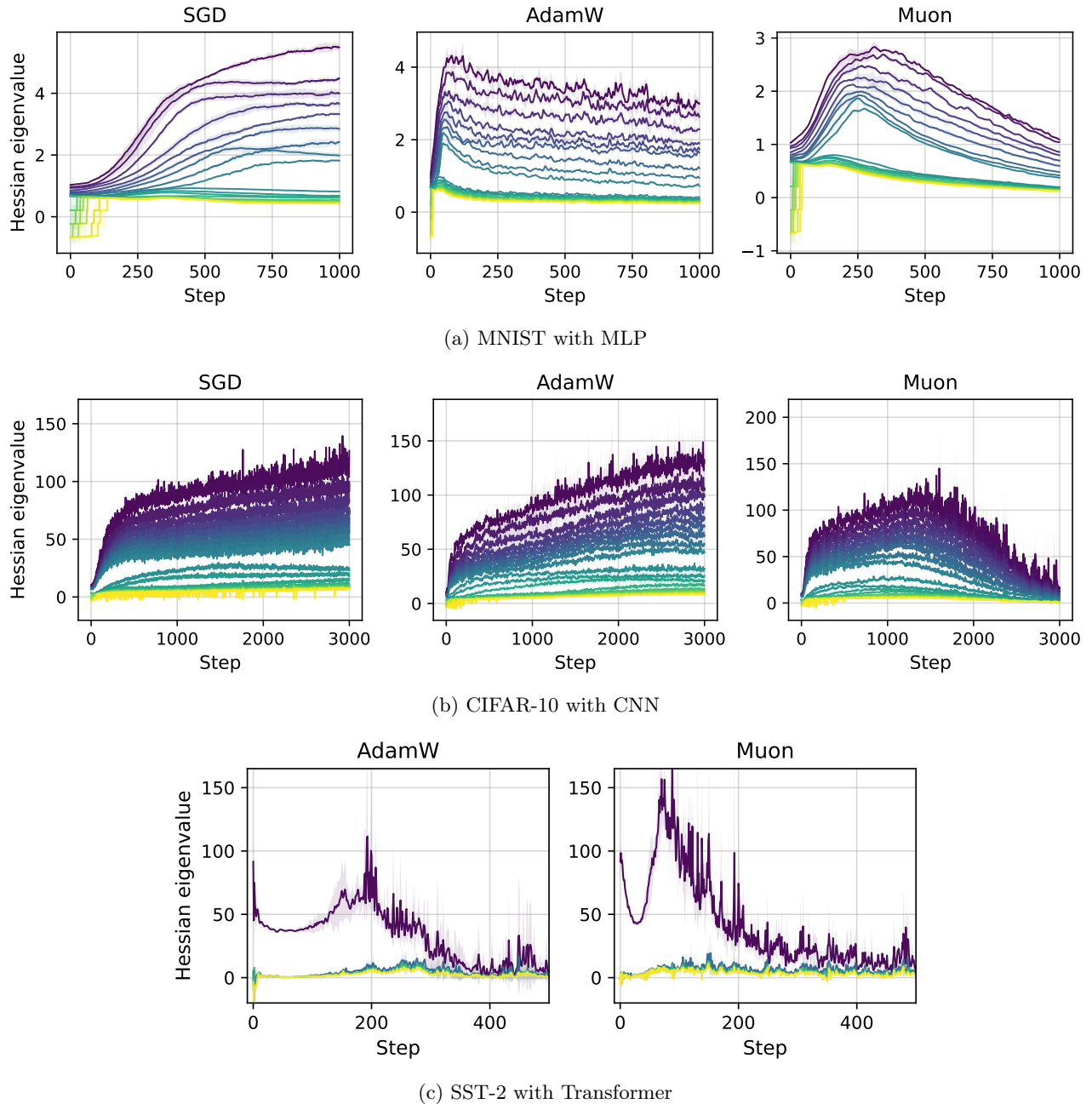
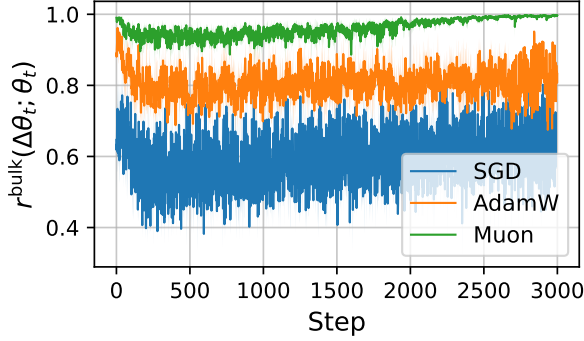
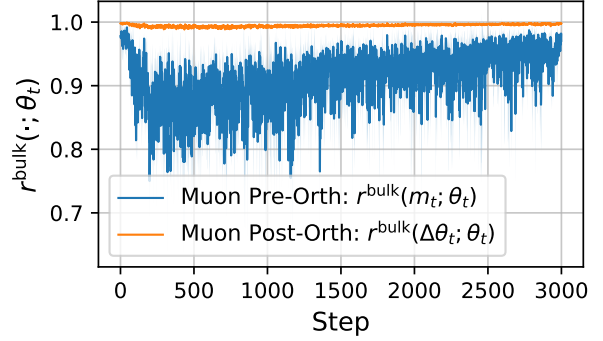


Figure 10: Eigenspectra of the loss Hessian across optimizers, datasets, and architectures. Across all cases, a small number of top- k eigenvalues, where k corresponds to the number of classes, form clear outliers, while the remaining eigenvalues are significantly smaller. This separation highlights a low-dimensional dominant subspace and a high-dimensional bulk subspace.

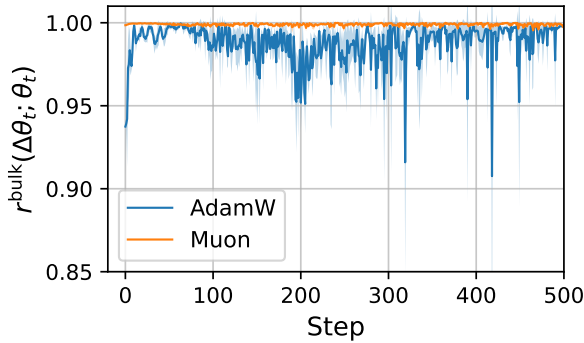


(a) Muon vs. SGD/AdamW

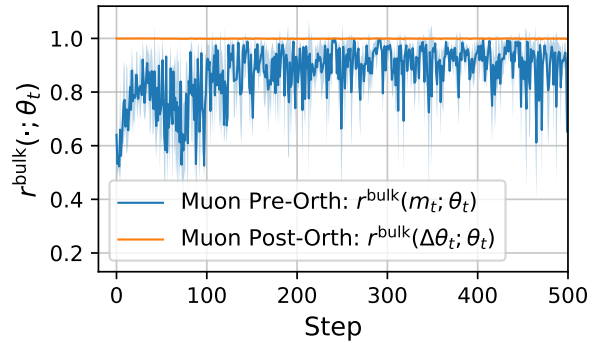


(b) Pre- vs. post-orthogonalization

Figure 11: Comparison of bulk component ratios on CIFAR-10 with CNN. Metrics are measured on a CIFAR-10 5k subset using a CNN architecture. (a) Muon consistently produces substantially larger bulk component updates than SGD and AdamW. (b) Muon’s orthogonalization increases the bulk ratio relative to the pre-orthogonalized momentum. Results are averaged over three runs.



(a) Muon vs. SGD/AdamW



(b) Pre- vs. post-orthogonalization

Figure 12: Comparison of bulk component ratios on SST-2 with Transformer. Metrics are measured on SST-2 using a Transformer architecture. (a) Muon consistently produces substantially larger bulk component updates than AdamW. (b) Muon’s orthogonalization increases the bulk ratio relative to the pre-orthogonalized momentum. Results are averaged over three runs.

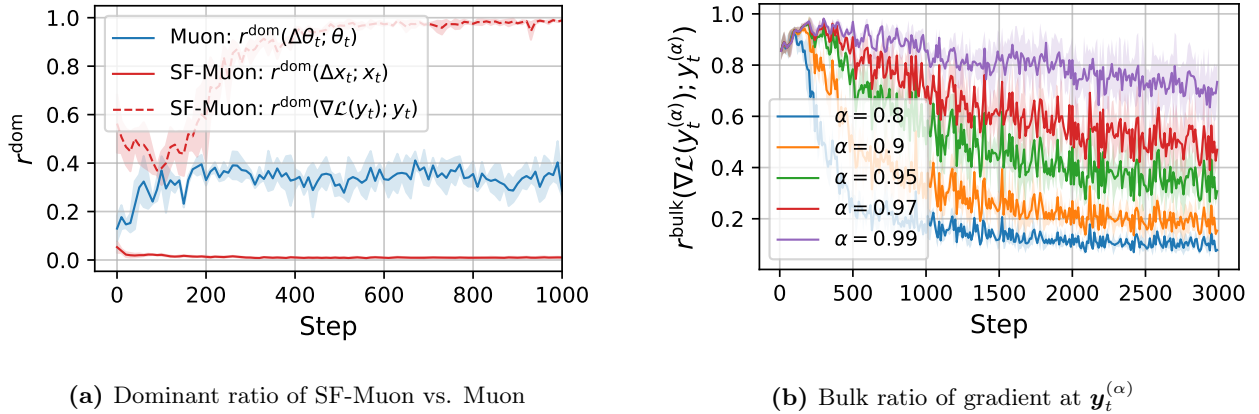


Figure 13: Comparison of dominant/bulk component ratios on CIFAR-10 with CNN. (a) Dominant ratios for Muon (blue) and SF-Muon (red). The solid and dashed red lines denote the dominant components of Δx_t and $\nabla\mathcal{L}(y_t)$, respectively. (b) Bulk ratios for gradients at $y_t^{(\alpha)} = (1 - \alpha)z_t + \alpha x_t$ across varying α , demonstrating that larger α values correlate with higher bulk components.

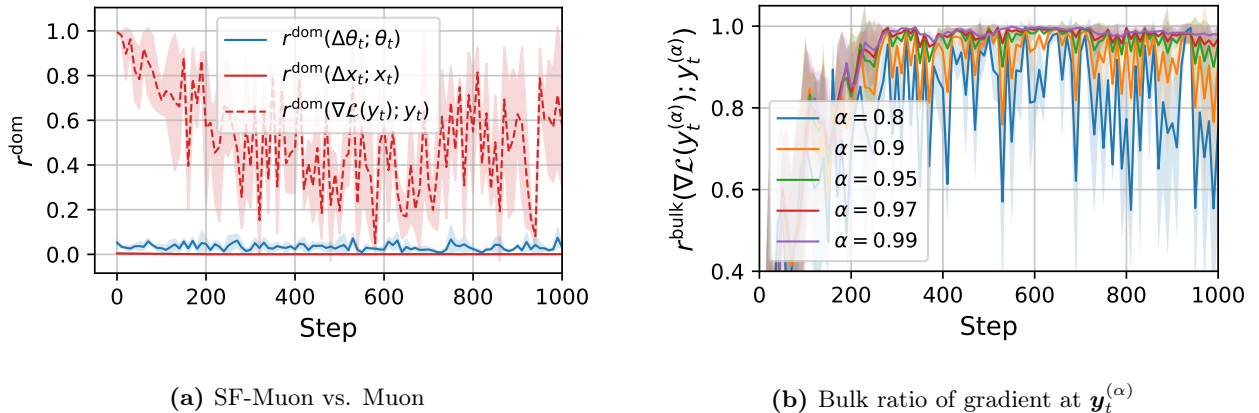


Figure 14: Comparison of dominant/bulk component ratios on SST-2 with Transformer. (a) Dominant ratios for Muon (blue) and SF-Muon (red). The solid and dashed red lines denote the dominant components of Δx_t and $\nabla\mathcal{L}(y_t)$, respectively. (b) Bulk ratios for gradients at $y_t^{(\alpha)} = (1 - \alpha)z_t + \alpha x_t$ across varying α , demonstrating that larger α values correlate with higher bulk components.

C Details for AMUSE

C.1 Algorithmic Description of AMUSE

In this section, we present the full procedure of AMUSE, summarized in Algorithm 1.

Algorithm 1 AMUSE: Anytime Muon with Stable Gradient Evaluation

Require: learning rate η , weight decay λ , AMUSE β_1 , AMUSE ρ , Muon momentum μ , AdamW second-moment coefficient β_2 , numerical constant ϵ , warmup step T_0

```

1: Initialize  $\mathbf{X}_1 \leftarrow \mathbf{Z}_1$ ,  $\mathbf{M}_0 \leftarrow \mathbf{0}$ ,  $\mathbf{V}_0 \leftarrow \mathbf{0}$ 
2: for  $t = 1, 2, \dots, T$  do
3:    $\eta_t \leftarrow \eta \cdot \min(1, t/T_0)$ 
4:    $c_{t+1} \leftarrow \frac{\eta_t^2}{\sum_{i=1}^t \eta_i^2}$ 
5:   if  $t \leq T_0$  then
6:      $\beta_1^{(t)} \leftarrow \beta_1$ 
7:   else
8:      $\beta_1^{(t)} \leftarrow 1 - \left(\frac{T_0 - 1}{t - 1}\right)^\rho (1 - \beta_1)$ 
9:   end if
10:   $\mathbf{Y}_t \leftarrow (1 - \beta_1^{(t)})\mathbf{Z}_t + \beta_1^{(t)}\mathbf{X}_t$ 
11:   $\mathbf{G}_t \leftarrow \nabla \mathcal{L}(\mathbf{Y}_t)$ 
12:  if parameter group uses Muon then
13:     $\mathbf{M}_t \leftarrow \mu\mathbf{M}_{t-1} + \mathbf{G}_t$ 
14:     $\mathbf{O}_t \leftarrow \text{Newton-Schulz}(\mathbf{M}_t)$ 
15:     $\mathbf{Z}_{t+1} \leftarrow (1 - \eta_t\lambda)\mathbf{Z}_t - \eta_t\mathbf{O}_t$ 
16:  else
17:     $\mathbf{V}_t \leftarrow \beta_2\mathbf{V}_{t-1} + (1 - \beta_2)(\mathbf{G}_t \odot \mathbf{G}_t)$ 
18:     $\widehat{\mathbf{V}}_t \leftarrow \mathbf{V}_t / (1 - \beta_2^t)$ 
19:     $\mathbf{U}_t \leftarrow \mathbf{G}_t \oslash \left(\sqrt{\widehat{\mathbf{V}}_t} + \epsilon\right)$ 
20:     $\mathbf{Z}_{t+1} \leftarrow (1 - \eta_t\lambda)\mathbf{Z}_t - \eta_t\mathbf{U}_t$ 
21:  end if
22:   $\mathbf{X}_{t+1} \leftarrow (1 - c_{t+1})\mathbf{X}_t + c_{t+1}\mathbf{Z}_{t+1}$ 
23: end for
24: return  $\mathbf{X}_{T+1}$ 

```

C.2 Averaging Orthogonalized Updates

We provide the derivation of the closed-form expression for the averaged sequence \mathbf{X}_t . This shows that the motion of \mathbf{X}_t is a weighted average of past orthogonalized Muon updates.

Recall that

$$\mathbf{Z}_{t+1} = \mathbf{Z}_t - \eta \mathcal{O}(\mathbf{M}_t), \quad \mathbf{X}_{t+1} = \left(1 - \frac{1}{t+1}\right) \mathbf{X}_t + \frac{1}{t+1} \mathbf{Z}_{t+1},$$

with initialization $\mathbf{Z}_1 = \mathbf{X}_1$. Since $c_{t+1} = 1/(t+1)$, the recursion for \mathbf{X}_t is the online average of the base iterates:

$$\mathbf{X}_t = \frac{1}{t} \sum_{i=1}^t \mathbf{Z}_i. \quad (6)$$

We verify this by induction. For $t = 1$, Eq. (6) holds since $\mathbf{X}_1 = \mathbf{Z}_1$. Assume that $\mathbf{X}_t = \frac{1}{t} \sum_{i=1}^t \mathbf{Z}_i$. Then

$$\begin{aligned} \mathbf{X}_{t+1} &= \left(1 - \frac{1}{t+1}\right) \mathbf{X}_t + \frac{1}{t+1} \mathbf{Z}_{t+1} \\ &= \frac{t}{t+1} \left(\frac{1}{t} \sum_{i=1}^t \mathbf{Z}_i\right) + \frac{1}{t+1} \mathbf{Z}_{t+1} \\ &= \frac{1}{t+1} \sum_{i=1}^{t+1} \mathbf{Z}_i. \end{aligned}$$

Thus Eq. (6) holds for all t .

Next, each base iterate can be written as

$$\mathbf{Z}_i = \mathbf{Z}_1 - \eta \sum_{j=1}^{i-1} \mathcal{O}(\mathbf{M}_j). \quad (7)$$

Substituting Eq. (7) into Eq. (6) gives

$$\begin{aligned} \mathbf{X}_t &= \frac{1}{t} \sum_{i=1}^t \left(\mathbf{Z}_1 - \eta \sum_{j=1}^{i-1} \mathcal{O}(\mathbf{M}_j) \right) \\ &= \mathbf{Z}_1 - \frac{\eta}{t} \sum_{i=1}^t \sum_{j=1}^{i-1} \mathcal{O}(\mathbf{M}_j). \end{aligned}$$

For a fixed j , the term $\mathcal{O}(\mathbf{M}_j)$ appears for $i = j+1, \dots, t$, hence $t-j$ times. Therefore,

$$\mathbf{X}_t = \mathbf{Z}_1 - \frac{\eta}{t} \sum_{j=1}^{t-1} (t-j) \mathcal{O}(\mathbf{M}_j). \quad (8)$$

We now derive the averaged-sequence update

$$\Delta \mathbf{X}_t := \mathbf{X}_{t+1} - \mathbf{X}_t.$$

Using Eq. (8),

$$\begin{aligned} \mathbf{X}_{t+1} &= \mathbf{Z}_1 - \frac{\eta}{t+1} \sum_{j=1}^t (t+1-j) \mathcal{O}(\mathbf{M}_j), \\ \mathbf{X}_t &= \mathbf{Z}_1 - \frac{\eta}{t} \sum_{j=1}^{t-1} (t-j) \mathcal{O}(\mathbf{M}_j). \end{aligned}$$

Thus,

$$\Delta \mathbf{X}_t = -\frac{\eta}{t+1} \sum_{j=1}^t (t+1-j) \mathcal{O}(\mathbf{M}_j) + \frac{\eta}{t} \sum_{j=1}^{t-1} (t-j) \mathcal{O}(\mathbf{M}_j).$$

For $j = 1, \dots, t-1$, the coefficient of $\mathcal{O}(\mathbf{M}_j)$ is

$$\eta \left(\frac{t-j}{t} - \frac{t+1-j}{t+1} \right) = -\frac{\eta j}{t(t+1)}.$$

For $j = t$, only the first sum contributes, giving

$$-\frac{\eta}{t+1} = -\frac{\eta t}{t(t+1)}.$$

Combining both cases,

$$\Delta \mathbf{X}_t = -\frac{\eta}{t(t+1)} \sum_{j=1}^t j \mathcal{O}(\mathbf{M}_j).$$

Therefore, \mathbf{X}_t averages the trajectory after orthogonalized Muon updates have been applied, and $\Delta \mathbf{X}_t$ is a weighted average of previous orthogonalized updates. This is distinct from momentum: momentum smooths gradients before orthogonalization, while \mathbf{X}_t averages the already orthogonalized updates.

C.3 Derivation of the β_t Schedule

In designing the schedule for β_t in AMUSE, one might initially consider a monotonically increasing schedule toward 1. However, following the derivation by Song et al. (2025b), a closer inspection of the schedule-free (SF) update reveals that the \mathbf{x}_t iterates perform an implicit averaging of the \mathbf{y}_t iterates:

$$\mathbf{x}_t = (1 - \omega_t) \mathbf{x}_{t-1} + \omega_t \mathbf{y}_t,$$

where the effective weight ω_t is given by:

$$\omega_t = \frac{1}{(t-1)(1-\beta_t) + 1}.$$

Crucially, if β_t increases too rapidly toward 1, the term $(1 - \beta_t)$ vanishes, causing the overall denominator to shrink and ω_t to increase. An increasing ω_t implies that the effective averaging window size actually *shrinks*. From an optimization perspective, shrinking the averaging window at later stages of training is highly counter-productive. Therefore, to prevent this adverse effect, we must establish a strict upper bound for β_t .

We define this upper bound by finding a schedule that strictly maintains the averaging window size—meaning ω_t remains constant—after a certain step T_0 . Setting $\omega_t = \omega_{T_0}$, we solve for the corresponding boundary β_t :

$$\begin{aligned} \omega_t &= \frac{1}{(t-1)(1-\beta_t) + 1} \\ &= \frac{1}{(T_0-1)(1-\beta_{T_0}) + 1} = \omega_{T_0}, \end{aligned}$$

which simplifies to:

$$\beta_t = 1 - \frac{T_0 - 1}{t - 1} (1 - \beta_{T_0}).$$

Building upon this boundary condition, we introduce an interpolation parameter ρ to control the rate of window growth. This parameter interpolates between the standard fixed- β schedule ($\beta_t = \beta_{T_0}$) and the constant-window boundary derived above, yielding our final schedule for $t \geq T_0$:

$$\beta_t = 1 - \left(\frac{T_0 - 1}{t - 1} \right)^\rho (1 - \beta_{T_0}).$$

By restricting $\rho \in [0, 1]$, we ensure a flexible design where the averaging window is allowed to grow ($0 \leq \rho < 1$) or at least remain constant ($\rho = 1$), effectively preventing it from ever shrinking.

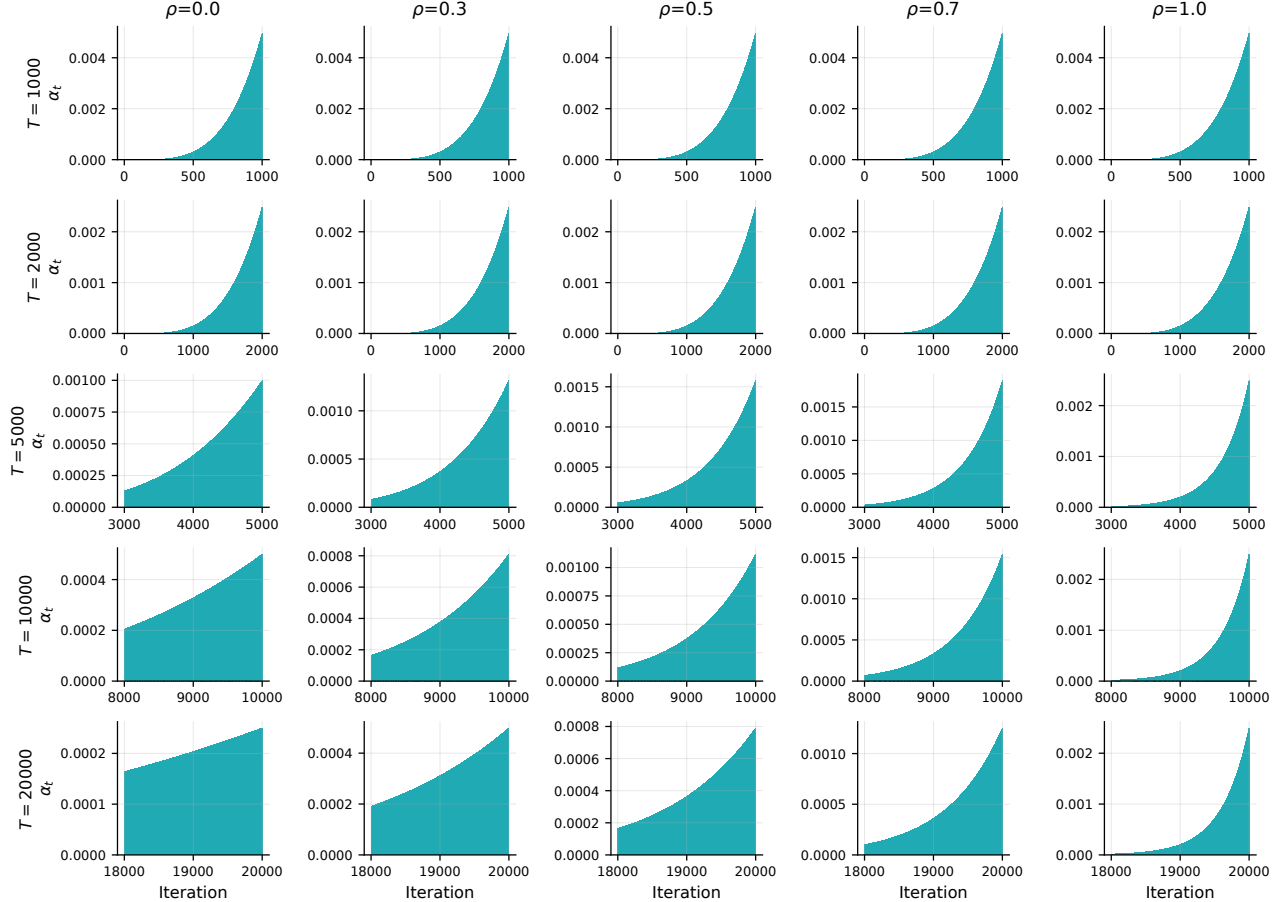


Figure 15: Effect of ρ on effective weights α_t . Histograms of α_t across varying sequence lengths T . For $T > T_0 = 2000$, lower ρ values allow the effective averaging window to continuously grow, whereas $\rho = 1$ strictly fixes the window to its size at T_0 .

Visualization of Averaging Window Size and β_t . To better understand the impact of our proposed schedule on the averaging dynamics, we visualize both the effective averaging window and the trajectory of β_t . By unrolling the recursive schedule-free update, the final evaluated parameter \mathbf{x}_T can be explicitly expressed as a weighted sum of all past iterates \mathbf{y}_t , i.e., $\mathbf{x}_T = \sum_{t=1}^T \alpha_t \mathbf{y}_t$, where the global effective weight α_t assigned to each step t is defined as:

$$\alpha_t \triangleq \frac{1}{(t-1)(1-\beta_t) + 1} \prod_{s=t+1}^T \left[\frac{(s-1)(1-\beta_s)}{(s-1)(1-\beta_s) + 1} \right].$$

This weight α_t directly dictates the size and shape of the effective averaging window. In Figure 15, we plot the histogram of these weights α_t (initialized with $\beta_1 = 0.8$) to illustrate how much “memory” the final model retains from past steps. The exact shape of this distribution is governed by the interpolation parameter ρ . Specifically, when $\rho = 0$, the schedule allows the averaging window size to continuously increase in a linear fashion throughout training. In contrast, setting $\rho = 1$ strictly fixes the window size after the initial warmup phase ($T_0 = 2000$). For any intermediate value ($0 < \rho < 1$), the schedule smoothly interpolates between these two extremes, providing a controlled, sub-linear growth of the memory window. Furthermore, we visualize the actual evolution of β_t over time in Figure 16.

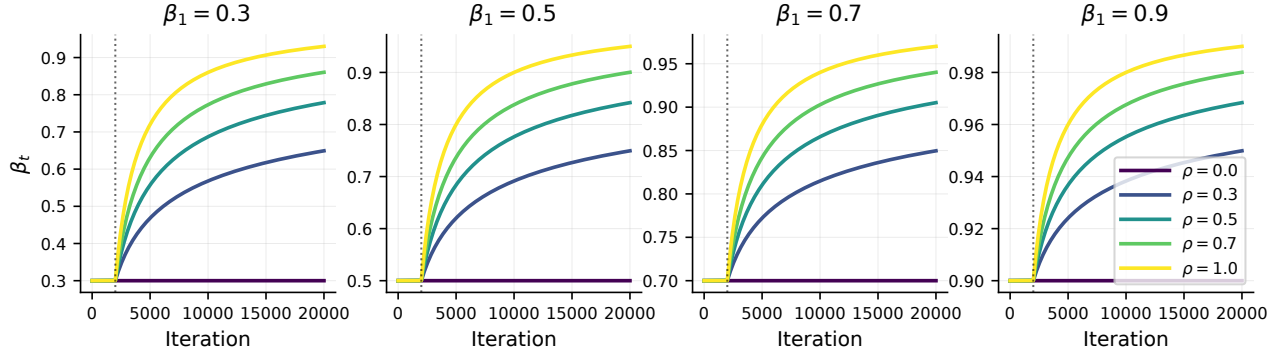


Figure 16: Evolution of β_t controlled by ρ . After the initial warmup phase ($T_0 = 2000$, dotted vertical line), ρ smoothly interpolates between a constant β baseline ($\rho = 0$) and the strict constant-window upper bound ($\rho = 1$).

C.4 Implementation Details

Averaging coefficient. In the main text, we use the simplified intuition $c_t = 1/t$. In the implementation, we follow the learning-rate-weighted averaging rule used in Defazio et al. (2024). Let η_t denote the effective learning rate at step t , including linear warmup. Rather than using a uniform average during warmup, we set

$$c_{t+1} = \frac{\eta_t^2}{\sum_{i=1}^t \eta_i^2}.$$

This prevents very early iterations, where the learning rate is small, from being overweighted in the averaged sequence. After warmup, η_t becomes constant and the coefficient recovers the usual $1/t$ -type decay.

Exact β_t schedule. In Appendix C.3, we use the simplified intuition $c_t = 1/t$ to derive the schedule for β_t . However, because c_t is not strictly equal to $1/t$ in practice, our actual implementation computes β_t using the generalized formulation based on the exact c_t :

$$\beta_t = 1 - \left(\frac{c_t(1 - c_{T_0})}{c_{T_0}(1 - c_t)} \right)^\rho (1 - \beta_{T_0}).$$

Batch normalization. Averaging methods, including Schedule-Free (Defazio et al., 2024), require special care for models with BatchNorm. During training, gradients are evaluated at the interpolated sequence \mathbf{Y}_t , so BatchNorm running statistics are accumulated for the training-time parameter state. During evaluation, however, the returned model is the averaged sequence \mathbf{X}_t . Therefore, the stored BatchNorm running statistics may not match the parameters used for evaluation.

For models with BatchNorm, we first convert the optimizer/model to the \mathbf{X}_t -state and then refresh BatchNorm statistics by forwarding a small number of training batches without gradient updates. This is analogous to PreciseBN-style recalibration (Wu and Johnson, 2021). No such step is needed for normalization layers that do not maintain batch-dependent running statistics, such as LayerNorm or RMSNorm, which are used in our language model experiments.

Weight decay. Following Defazio et al. (2024), weight decay may be applied either to the gradient-evaluation sequence \mathbf{y}_t or to the base sequence \mathbf{z}_t . In our implementation, we apply the standard weight-decay term to \mathbf{z}_t . We keep decay at \mathbf{y}_t as a separate optional variant, but do not use it unless explicitly stated.

Computational resources. We use up to 8 NVIDIA RTX A6000 GPUs for the image-domain experiments and the 124M Llama experiments. For experiments at the 720M scale and above, we use up to 8 NVIDIA A100 GPUs with data-parallel training.

D Image Domain Experiments

D.1 Experimental Details

For the image-domain experiments, we mostly follow the experimental setup of Defazio et al. (2024). We additionally include Muon as a new baseline and add the ISIC 2018 image segmentation task.

We follow the standard Muon hybrid setup (Jordan et al., 2024): Muon is applied to hidden matrix-valued layers, while SGD with momentum is used for non-Muon parameters. Only for MAE fine-tuning in image domain experiments, we instead use the Muon+AdamW hybrid setup commonly used for Transformer models (Jordan et al., 2024; Liu et al., 2025a): Muon is applied to the hidden-layer weight matrices of the ViT backbone, while AdamW is used for the classifier head and all one-dimensional parameters, including biases and LayerNorm parameters.

When available, we use the tuned hyperparameters reported by Defazio et al. (2024) for SGD, SF-SGD, AdamW, and SF-AdamW. For the added baseline Muon, we tune the learning rate, weight decay, and Muon momentum following the same tuning protocol. For vanilla Muon, we also tune the learning rate of the auxiliary SGD optimizer separately, since using the same learning rate for Muon and SGD led to poor performance.

For AMUSE, we fix the Muon momentum to 0.95 and use the same learning rate for the auxiliary SGD optimizer, reducing the number of tuned hyperparameters. In the Muon+SGD image-domain setting, AMUSE uses SGD without momentum for the non-Muon parameters (SF-SGD update for non-Muon parameters). For MAE fine-tuning, we use Muon with AdamW for non-Muon parameters, AMUSE uses AdamW without first momentum and we fix the second-moment coefficient to $\beta_2 = 0.999$ (SF-AdamW update for non-Muon parameters). Thus, beyond the base learning rate and weight decay, AMUSE only additionally adjusts the AMUSE-specific parameters β_1 and ρ .

CIFAR-10. We train a Wide-ResNet-16-8 architecture (Zagoruyko and Komodakis, 2016) on the CIFAR-10 image classification (Krizhevsky et al., 2009) dataset. We use a batch size of 128 and train for 300 epochs.

Table 4: Hyperparameters for CIFAR-10.

SGD and SF-SGD			Muon and AMUSE		
Hyperparameter	SGD	SF-SGD	Hyperparameter	Muon	AMUSE
Epochs		300	Epochs		300
Batch size		128	Batch size		128
Warmup ratio		0.05	Warmup ratio		0.05
Seeds		5	Seeds		5
Learning Rate	0.2	10.0	Muon LR	0.05	0.2
Weight decay	0.0001	0.0001	SGD LR	0.0001	0.2
SGD momentum β	0.9	–	Weight decay	0.01	0.02
SF-SGD β_1	–	0.9	Muon momentum μ	0.9	0.95
LR decay scheduler	cosine	–	SGD momentum β	0.9	–
			AMUSE β_1	–	0.8
			AMUSE ρ	–	0.3
			LR decay scheduler	cosine	–

CIFAR-100. We train a DenseNet architecture (Huang et al., 2017) on the CIFAR-100 image classification dataset. We use a batch size of 128 and train for 300 epochs.

Table 5: Hyperparameters for CIFAR-100.

SGD and SF-SGD			Muon and AMUSE		
Hyperparameter	SGD	SF-SGD	Hyperparameter	Muon	AMUSE
Epochs		300	Epochs		300
Batch size		64	Batch size		64
Warmup ratio		0.05	Warmup ratio		0.05
Seeds		5	Seeds		5
Learning Rate	0.05	5.0	Muon LR	0.05	0.5
Weight decay	0.0002	0.0002	SGD LR	0.001	0.5
SGD momentum β	0.9	–	Weight decay	0.005	0.002
SF-SGD β_1	–	0.9	Muon momentum μ	0.9	0.95
LR decay scheduler	cosine	–	SGD momentum β	0.9	–
			AMUSE β_1	–	0.7
			AMUSE ρ	–	0.4
			LR decay scheduler	cosine	–

SVHN. We train a ResNet-3-96 architecture (He et al., 2016) on the Street View House Numbers (SVHN) dataset (Netzer et al., 2011). We use a batch size of 32 and train for 300 epochs.

Table 6: Hyperparameters for SVHN.

SGD and SF-SGD			Muon and AMUSE		
Hyperparameter	SGD	SF-SGD	Hyperparameter	Muon	AMUSE
Epochs		300	Epochs		300
Batch size		32	Batch size		32
Warmup ratio		0.05	Warmup ratio		0.05
Seeds		5	Seeds		5
Learning Rate	0.1	1.0	Muon LR	0.05	0.1
Weight decay	0.0001	0.0002	SGD LR	0.001	0.1
SGD momentum β	0.9	–	Weight decay	0.002	0.01
SF-SGD β_1	–	0.9	Muon momentum μ	0.9	0.95
LR decay scheduler	cosine	–	SGD momentum β	0.9	–
			AMUSE β_1	–	0.85
			AMUSE ρ	–	0.2
			LR decay scheduler	cosine	–

ImageNet-1k. We train a ResNet-50 architecture (He et al., 2016) on the ILSVRC 2012 (Russakovsky et al., 2015) ImageNet-1k classification dataset. We use a batch size of 256 and train for 100 epochs.

Table 7: Hyperparameters for ImageNet-1k.

SGD and SF-SGD			Muon and AMUSE		
Hyperparameter	SGD	SF-SGD	Hyperparameter	Muon	AMUSE
Epochs		100	Epochs		100
Batch size		256	Batch size		256
Warmup ratio		0.05	Warmup ratio		0.05
Seeds		5	Seeds		5
Learning Rate	0.05	1.5	Muon LR	0.1	0.5
Weight decay	0.0001	0.00005	SGD LR	0.00001	0.5
SGD momentum β	0.9	–	Weight decay	0.001	0.0005
SF-SGD β_1	–	0.9	Muon momentum μ	0.9	0.95
LR decay scheduler	cosine	–	SGD momentum β	0.9	–
			AMUSE β_1	–	0.6
			AMUSE ρ	–	0.8
			LR decay scheduler	cosine	–

ISIC 2018. We train a base U-Net architecture (Ronneberger et al., 2015) on the ISIC 2018 dataset (Codella et al., 2019) for binary medical image segmentation. We use a batch size of 8 and train for 50 epochs. Our implementation is based on the U-Bench codebase².

Since this setup is newly added in our paper, we extensively tune the learning rate, weight decay, and momentum for each baseline. For vanilla Muon, we additionally tune the auxiliary SGD learning rate used for non-Muon parameters.

Table 8: Hyperparameters for ISIC 2018.

SGD and SF-SGD			Muon and AMUSE		
Hyperparameter	SGD	SF-SGD	Hyperparameter	Muon	AMUSE
Epochs		50	Epochs		50
Batch size		8	Batch size		8
Warmup ratio		0.05	Warmup ratio		0.05
Seeds		5	Seeds		5
Learning Rate	0.02	2e-3	Muon LR	0.01	0.2
Weight decay	0.0005	0.01	SGD LR	0.001	0.2
SGD momentum β	0.9	–	Weight decay	0.001	0.05
SF-SGD β_1	–	0.9	Muon momentum μ	0.9	0.95
LR decay scheduler	cosine	–	SGD momentum β	0.9	–
			AMUSE β_1	–	0.6
			AMUSE ρ	–	0.2
			LR decay scheduler	cosine	–

MAE. We fine-tune a pretrained MAE ViT-Base model (vit_base_patch16) on ImageNet-1K for 100 epochs. The model uses 16×16 patches and the standard ViT-Base architecture with 12 transformer blocks, hidden size 768, and 12 attention heads.

All runs use the same AdamW-pretrained MAE pretrained initialization and differ only in optimizer-specific hyperparameters. Since MAE fine-tuning starts from an AdamW-pretrained checkpoint, we carefully tune the initial interpolation value β_1 for AMUSE. We use smaller β_1 values than in the other experiments to avoid a large early discrepancy between the base sequence and the averaged sequence, allowing the base trajectory to adapt smoothly to the fine-tuning objective. Our implementation uses the official mae code³.

²<https://github.com/FengheTan9/U-Bench>

³<https://github.com/facebookresearch/mae>

Table 9: Hyperparameters for MAE fine-tuning.

AdamW and SF-AdamW			Muon and AMUSE		
Hyperparameter	AdamW	SF-AdamW	Hyperparameter	Muon	AMUSE
Epochs		100	Epochs		100
Batch size		256	Batch size		256
Warmup ratio		0.05	Warmup ratio		0.05
Learning rate	5e-4	2e-3	Learning rate	5e-4	2e-3
Weight decay	0.05	0.05	Weight decay	0.01	0.05
AdamW β_1	0.9	–	Muon momentum	0.95	0.95
SF-AdamW β_1	–	0.9	AdamW β_1	0.9	–
AdamW β_2	0.999	0.999	AMUSE β_1	–	0.4
LR decay scheduler	cosine	–	AdamW β_2	0.999	0.999
Drop Path		0.1	AMUSE ρ	–	0.3
Reprob		0.25	LR decay scheduler	cosine	–
Mixup		0.8	Drop Path		0.1
Cutmix		1.0	Reprob		0.25
			Mixup		0.8
			Cutmix		1.0

E Large Language Model Experiments

E.1 Architecture Details

Our experimental setup follows [Semenov et al. \(2026\)](#), using their public codebase.⁴ We use three decoder-only Llama-style models with approximately 124M, 720M, and 1B parameters. Across all model sizes, we use a sequence length of 512, the GPT-2 tokenizer with vocabulary size 50,304, RMSNorm with $\epsilon = 10^{-5}$, bias-free projections, SwiGLU MLPs with `multiple_of=256`, no dropout, and bfloat16 training. Table 10 summarizes the model-specific dimensions.

Table 10: Model configurations for LLM experiments.

Model size	Layers	Attention heads	Hidden size
124M	12	12	768
720M	12	16	2048
1B	24	28	1792

E.2 Hyperparameter Tuning

For AdamW, D-Muon, and SF-AdamW baselines, we follow the hyperparameter search spaces reported by [Semenov et al. \(2026\)](#). At the 124M scale, their tuning includes learning rate, warmup steps, weight decay, learning-rate scheduler, gradient clipping, and optimizer-specific momentum parameters. For AdamW, the searched optimizer-specific parameters are β_1 and β_2 . For Muon (D-Muon), the search includes learning rate, Muon momentum, AdamW hyperparameters for one-dimensional parameters, and whether to use Nesterov momentum. For SF-AdamW, the search includes learning rate, warmup length, weight decay, gradient clipping, and the Schedule-Free AdamW parameters β_1 and β_2 , without a learning-rate decay schedule.

For AMUSE, we do not introduce additional tuning of the optimizer momentum parameters. We fix the Muon momentum $\mu = 0.95$, and keep the AdamW’s β_2 for non-Muon parameters fixed to 0.999 to avoid additional hyperparameter tuning. We tune hyperparameters introduced by AMUSE: the initial interpolation value β_1 and ρ . Specifically, we sweep $\beta_1 \in \{0.4, 0.6\}$ and $\rho \in \{0.6, 0.8\}$. Across our experiments, $\rho = 0.8$ consistently performs well.

Due to computational limitations, we do not perform additional hyperparameter tuning for the 1B-scale experiments. For all optimizers, we directly use the best hyperparameters from the 720M setting. We also provide the AMUSE hyperparameter search grid in Table 14.

⁴<https://github.com/epfml/llm-optimizer-benchmark>

E.2.1 Hyperparameters for 124M parameters model

Table 11: Selected hyperparameters at the 124M scale.

AdamW and Muon (D-Muon)			SF-AdamW and AMUSE		
Hyperparameter	AdamW	Muon	Hyperparameter	SF-AdamW	AMUSE
Learning rate	0.001	0.002	Learning rate	0.002	0.01
Batch size	256	256	Batch size	256	256
Sequence length	512	512	Sequence length	512	512
Warmup steps	2000	2000	Warmup steps	8000	6000
Weight decay	0.1	0.1	Weight decay	0.1	0.1
Gradient clipping	0.5	0.5	Gradient clipping	0.5	0.5
AdamW β_1	0.8	0.8	AMUSE β_1	-	0.6
AdamW β_2	0.999	0.999	AMUSE ρ	-	0.8
Muon momentum	-	0.95	SF-AdamW β_1	0.9	-
LR decay scheduler	cosine	cosine	AdamW β_2	0.9999	0.999
			Muon momentum	-	0.95
			LR decay scheduler	-	-

E.2.2 Hyperparameters for 720M parameters model

Table 12: Selected hyperparameters at the 720M scale.

AdamW and Muon (D-Muon)			SF-AdamW and AMUSE		
Hyperparameter	AdamW	Muon	Hyperparameter	SF-AdamW	AMUSE
Learning rate	0.001	0.001	Learning rate	0.001	0.01
Batch size	1984	1984	Batch size	1984	1984
Sequence length	512	512	Sequence length	512	512
Warmup steps	2000	2000	Warmup steps	8000	2000
Weight decay	0.1	0.1	Weight decay	0.1	0.1
Gradient clipping	0.1	0.1	Gradient clipping	0.1	0.1
AdamW β_1	0.9	0.9	AMUSE β_1	-	0.4
AdamW β_2	0.999	0.99	AMUSE ρ	-	0.8
Muon momentum	-	0.95	SF-AdamW β_1	0.9	-
LR decay scheduler	cosine	cosine	AdamW β_2	0.9999	0.999
			Muon momentum	-	0.95
			LR decay scheduler	-	-

E.2.3 Hyperparameters for 1B parameters model

Table 13: Selected hyperparameters at the 1B scale.

AdamW and Muon (D-Muon)			SF-AdamW and AMUSE		
Hyperparameter	AdamW	Muon	Hyperparameter	SF-AdamW	AMUSE
Learning rate	0.001	0.001	Learning rate	0.001	0.01
Batch size	2048	2048	Batch size	2048	2048
Sequence length	512	512	Sequence length	512	512
Warmup steps	2000	2000	Warmup steps	8000	2000
Weight decay	0.1	0.1	Weight decay	0.1	0.1
Gradient clipping	0.1	0.1	Gradient clipping	0.1	0.1
AdamW β_1	0.9	0.9	AMUSE β_1	–	0.4
AdamW β_2	0.999	0.99	AMUSE ρ	–	0.8
Muon momentum	–	0.95	SF-AdamW β_1	0.9	–
LR decay scheduler	cosine	cosine	AdamW β_2	0.9999	0.999
			Muon momentum	–	0.95
			LR decay scheduler	–	–

E.2.4 Search grid table for AMUSE

For AdamW, SF-AdamW, and Muon (D-Muon), we use the best reported hyperparameters from the LLM optimizer benchmark of [Semenov et al. \(2026\)](#); their full search grids are provided in their work. We tune AMUSE separately and report our search grid below.

Table 14: AMUSE hyperparameter search grid for LLM pretraining. Selected values are shown in bold.

Scale	Hyperparameter	Search grid
124M	Learning rate	0.002, 0.005, 0.01 , 0.02
	Batch size	256
	Sequence length	512
	Warmup steps	2000, 4000, 6000
	Weight decay	0.01, 0.05 , 0.1
	Gradient clipping	0.5
	AMUSE β_1	0.4, 0.6
	AMUSE ρ	0.6, 0.8
720M	Learning rate	0.002, 0.005, 0.01 , 0.02
	Batch size	1984
	Sequence length	512
	Warmup steps	2000
	Weight decay	0.1
	Gradient clipping	0.1
	AMUSE β_1	0.4 , 0.6
	AMUSE ρ	0.8
1B	Learning rate	0.01
	Batch size	2048
	Sequence length	512
	Warmup steps	2000
	Weight decay	0.1
	Gradient clipping	0.1
	AMUSE β_1	0.4
AMUSE ρ	0.8	

Fixed across sweeps: AdamW $\beta_2 = 0.999$, Muon momentum 0.95, no LR decay.

F Additional Experiments

F.1 Comparison with Additional Optimizer Baselines

We first compare AMUSE with other strong optimizer baselines for 124M Llama pretraining. In addition to AdamW, Muon, and SF-AdamW, we include AdEMAMix, ADOPT, Signum, Prodigy, MARS, Lion, Sophia, and SOAP, using the tuned hyperparameters reported by [Semenov et al. \(2026\)](#). As shown in Figure 17, AMUSE achieves the best validation perplexity among these optimizers, indicating that its advantage is not limited to the main baselines considered in the paper.

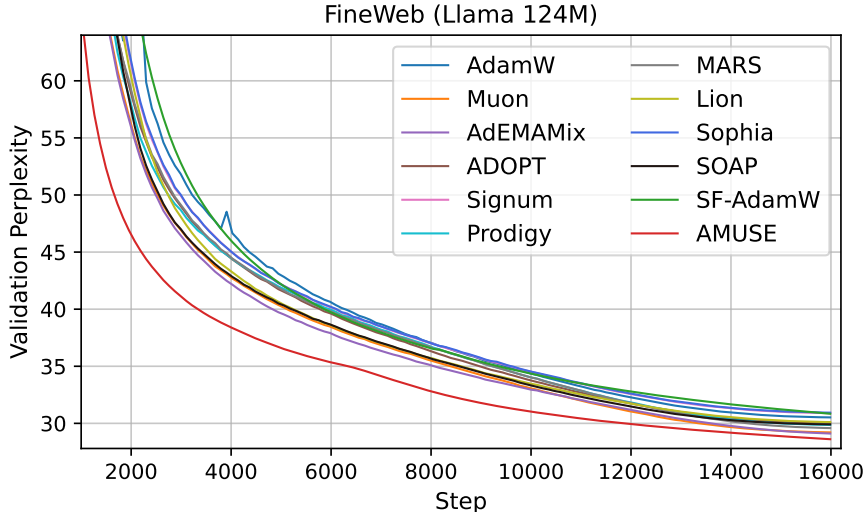


Figure 17: Comparison with Other Baselines on Llama 124M model.

F.2 Comparison with Muon with EWA and WSD

We further compare AMUSE with Muon equipped with exponential weight averaging (EWA) and warmup-stable-decay (WSD). These baselines test whether the gains of AMUSE can be matched by adding an external averaging mechanism or an explicit decay phase to constant-LR Muon.

For the 124M Llama experiment, we tune constant-LR Muon over learning rate, warmup steps, and weight decay, while keeping the momentum parameters the same as in the cosine-decay Muon baseline. The best constant-LR Muon setting uses learning rate 10^{-3} , weight decay 0.05, and 1000 warmup steps. We apply EWA with multiple averaging coefficients ($\alpha = 0.99, 0.999, 0.9995$) to this tuned constant-LR Muon trajectory, and also run WSD-style decay phases for 2k iterations starting from multiple Muon checkpoints.

As shown in Figure 18, both EWA and WSD improve constant-LR Muon. EWA gives better validation perplexity with stronger averaging, and applying a 2k-step decay phase from Muon checkpoints substantially lowers perplexity. However, none of the EWA variants or WSD decay runs matches the performance of AMUSE, and AMUSE remains better throughout training. This suggests that AMUSE does not merely imitate post-hoc averaging or learning-rate decay, but instead maintains a more stable trajectory during training while preserving fast progress.

For ImageNet, we additionally evaluate Muon with EWA using the same EWA coefficient grid. In this experiment, we use the optimal hyperparameters of the cosine-scheduled Muon baseline and apply EWA. As shown in Figure 19, Muon+EWA does not outperform AMUSE for any averaging coefficient. This suggests that AMUSE does not merely behave like an external weight average or a learning-rate decay, but instead maintains a more stable trajectory during training.

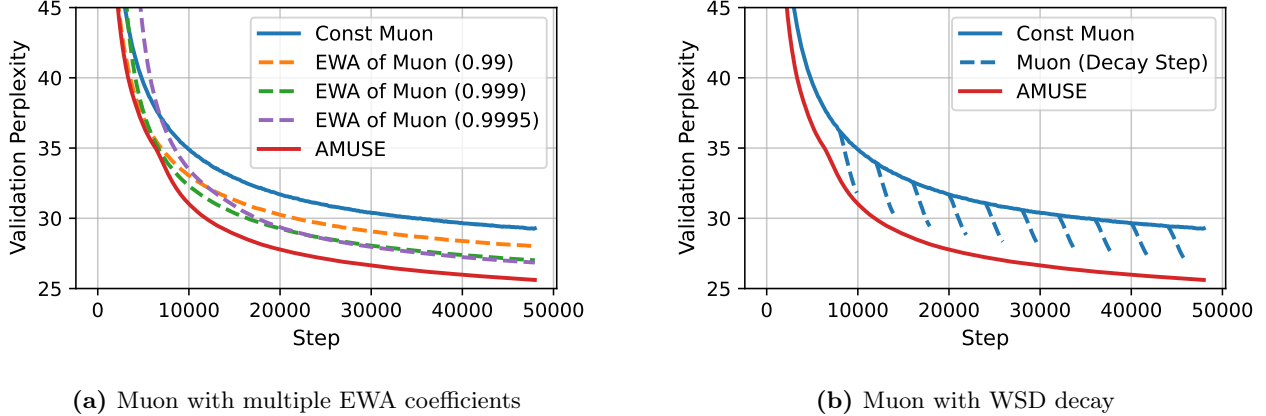


Figure 18: Comparison with Muon+EWA and Muon+WSD on 124M Llama pretraining. Left: we apply exponential weight averaging (EWA) with multiple averaging coefficients to the tuned constant-LR Muon trajectory. Right: we apply 2k-step WSD-style decay phases starting from multiple Muon checkpoints. Both EWA and WSD improve constant-LR Muon, but none of these variants matches AMUSE.

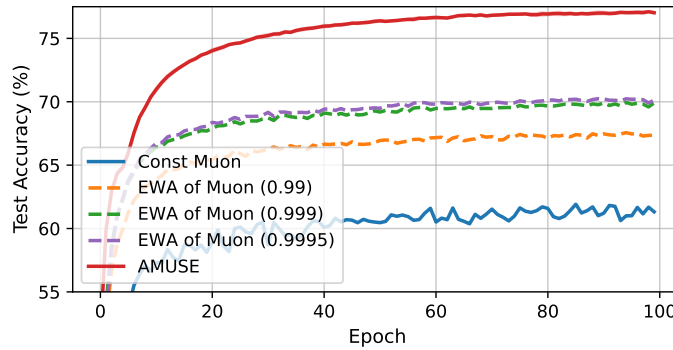


Figure 19: Comparison with Muon with EWA on ImageNet.

F.3 Longer Training Result

We further train AMUSE and the main baselines for a longer horizon, corresponding to the $3\times$ Chinchilla token budget. As shown in Figure 20, AMUSE continues to achieve the lowest validation perplexity on the 124M Llama model without additional hyperparameter tuning. Notably, AMUSE maintains its advantage even without an explicit learning-rate decay schedule, suggesting that its averaged trajectory remains effective beyond the standard training horizon.

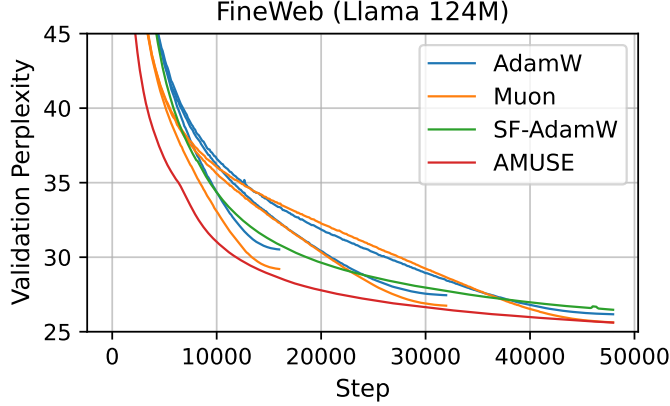


Figure 20: Longer-horizon training results on 124M Llama pretraining. We train AMUSE and the main baselines for the $3\times$ Chinchilla token budget. AMUSE achieves the lowest validation perplexity throughout the extended training horizon, even without using an explicit learning-rate decay schedule.

F.4 Hyperparameter Sensitivity.

Figure 21 and Table 15 show the sensitivity of AMUSE to β_1 and ρ in the 124M Llama setting. AMUSE shows only mild variation in validation perplexity across the tested ranges. Moreover, every swept configuration achieves lower perplexity than the tuned Muon baseline with cosine learning-rate decay.

Table 15: Hyperparameter sensitivity of AMUSE on 124M Llama pretraining.

Sweep	Hyperparameter value	Validation perplexity
β_1 sweep, $\rho = 0.8$	0.4	28.81
	0.5	28.70
	0.6	28.61
	0.7	28.73
ρ sweep, $\beta_1 = 0.6$	0.6	28.79
	0.7	28.68
	0.8	28.61
	0.9	28.63
Muon with cosine decay	–	29.21

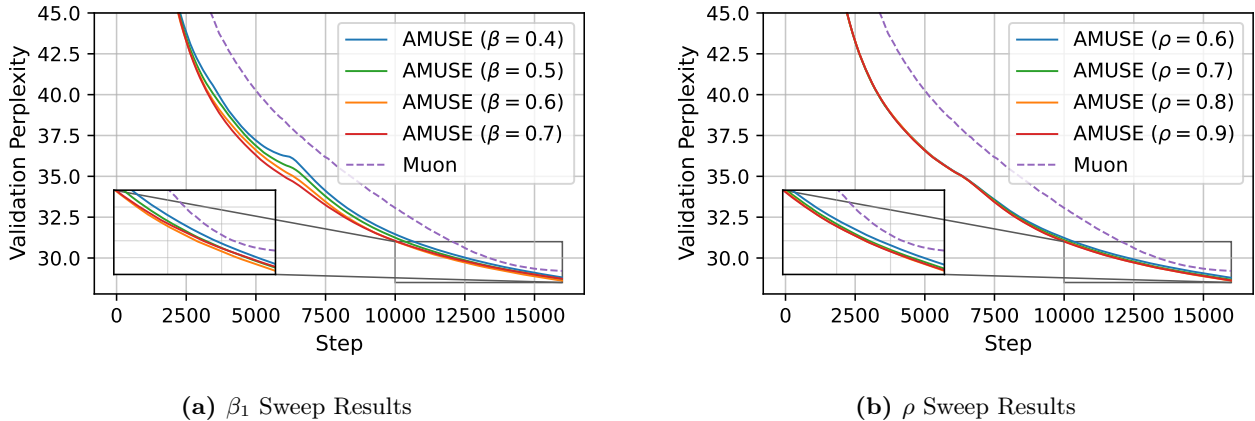


Figure 21: Hyperparameter sensitivity varying β_1 and ρ on 124M Llama pretraining.

F.5 Wall-clock Time Comparison

We compare the per-iteration wall-clock time of different optimizers in the 124M Llama pretraining setting. Following common practice in optimizer runtime comparisons, we report the average training iteration time, including forward pass, backward pass, and optimizer update. All optimizers are evaluated with the same model, sequence length, global batch size, precision, hardware, and distributed training configuration. AMUSE has a per-iteration cost similar to Muon, while SF-AdamW has a per-iteration cost similar to AdamW. The main runtime difference between these two groups comes from the Newton–Schulz iterations used to orthogonalize Muon updates, which are also used by AMUSE for Muon-updated layers.

Table 16: Wall-clock time comparison on 124M Llama pretraining. We report average iteration time after discarding warmup iterations. Each iteration processes 256×512 tokens. Relative time is normalized by AdamW.

Optimizer	Iter. time (s)	Relative time	Throughput (tokens/s)
AdamW	0.674	1.00×	177423
SF-AdamW	0.684	1.015	175213
Muon	0.706	1.047	169222
AMUSE	0.719	1.067	166697

F.6 Ablation Studies

Comparison with SF-Muon. We compare AMUSE with fixed- β SF-Muon. SF-Muon is tuned over the same hyperparameter grid, including multiple fixed β values. As shown in Figures 22 and 23, fixed- β SF-Muon does not outperform AMUSE in either setting. In particular, its improvement becomes limited in the later stage of training, suggesting that a fixed gradient-evaluation point cannot maintain the same early-speed and late-stability trade-off as AMUSE. By gradually increasing β_t , AMUSE continues to make progress later in training while preserving stable optimization.

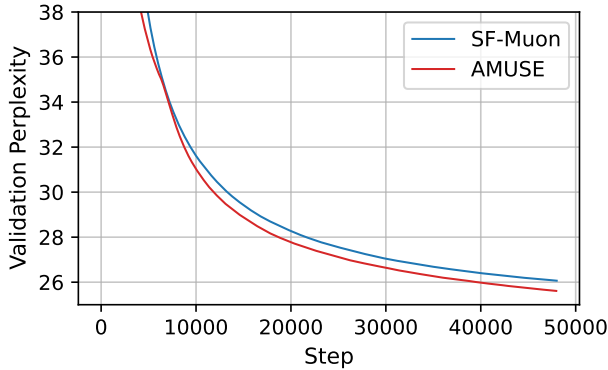


Figure 22: Comparison between AMUSE and fixed- β SF-Muon on 124M Llama pretraining. We compare AMUSE with SF-Muon using the best fixed interpolation value, $\beta = 0.95$. Fixed- β SF-Muon makes progress early in training but its improvement becomes limited in the later stage. In contrast, AMUSE continues to improve by gradually moving the gradient-evaluation point toward the averaged trajectory.

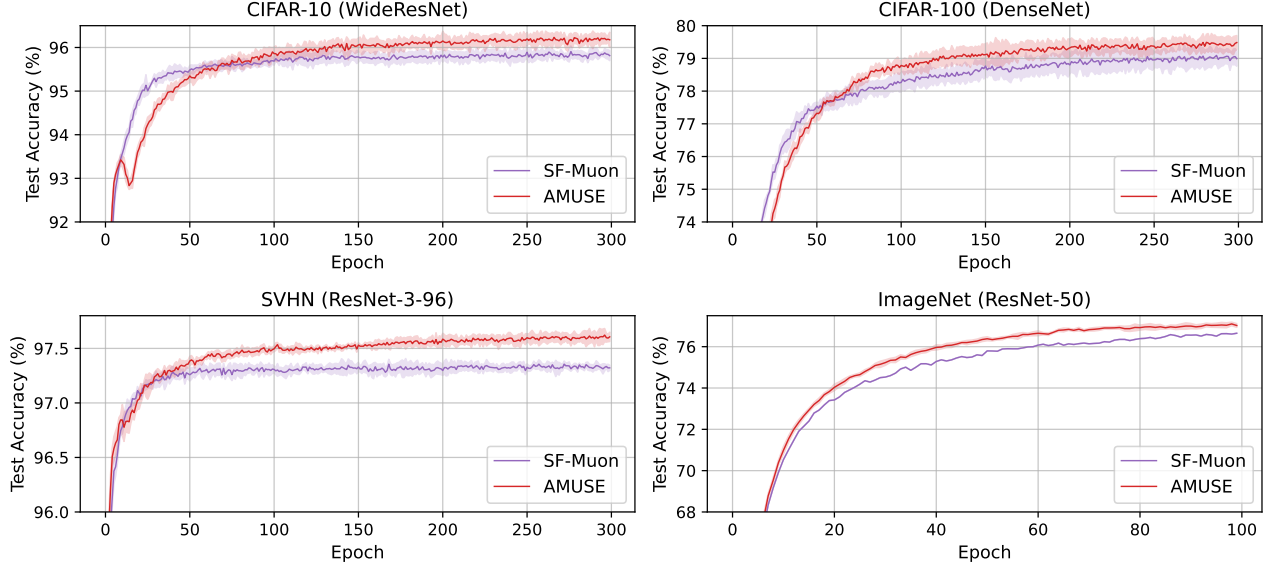


Figure 23: Comparison between AMUSE and fixed- β SF-Muon on Image domain experiments. We compare AMUSE with SF-Muon in image classification benchmarks. Runs are averaged over five random seeds, except for ImageNet trained with SF-Muon due to computation constraints.

AMUSE without Muon Momentum. To examine the role of Muon momentum in AMUSE and SF-Muon, we remove the momentum buffer used before the orthogonalization step. As shown in Figure 24, removing Muon momentum causes a large performance drop for both methods. This indicates that momentum is crucial for Muon-based optimization: it smooths stochastic gradient noise before orthogonalization and accumulates a more reliable update direction, including useful bulk components. Without momentum, the orthogonalization step can amplify noisy components, resulting in less stable and less effective training.

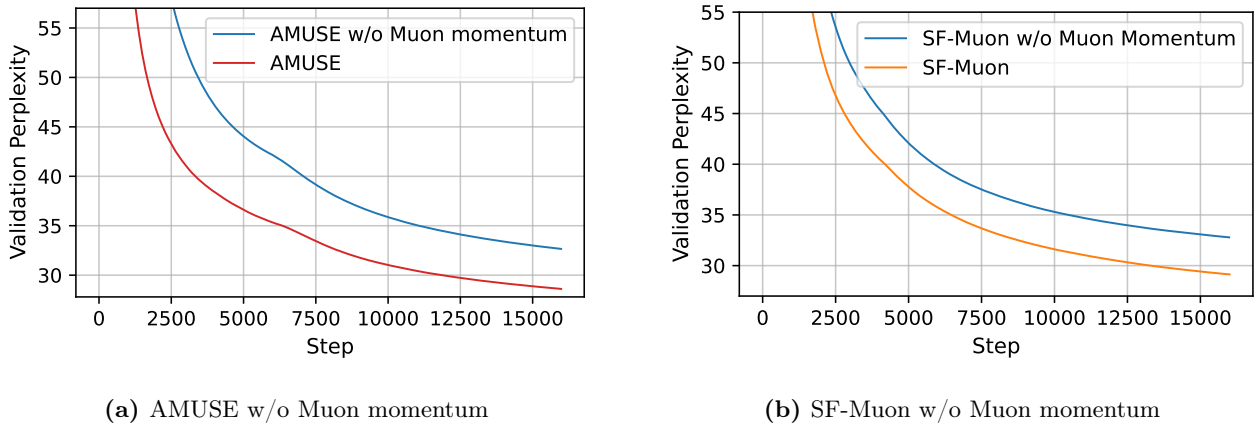


Figure 24: Momentum ablation on 124M Llama pretraining. We compare each method with and without Muon momentum, keeping all other hyperparameters fixed. Removing Muon momentum substantially degrades both AMUSE and SF-Muon, showing that momentum is essential for stable Muon-based optimization.

Can We Stop Increasing β_t After It Becomes Large? We further test whether AMUSE’s improvement comes only from reaching a specific large interpolation value. To do so, we use the best hyperparameter for AMUSE, $\beta_1 = 0.6$ and $\rho = 0.8$, but cap β_t at the best fixed value used by SF-Muon, $\beta = 0.95$. That is, after β_t reaches 0.95, we keep it fixed instead of allowing it to continue increasing toward 1.

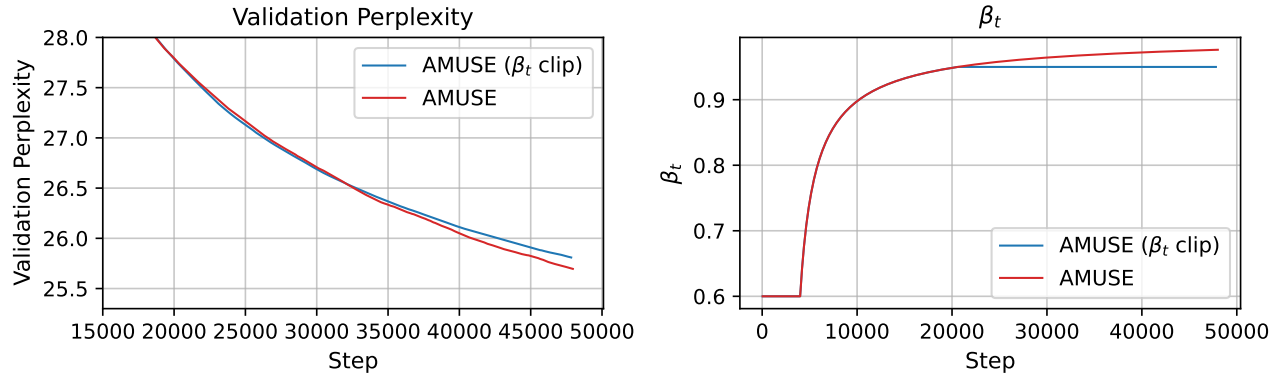


Figure 25: Effect of stopping the increase of β_t in AMUSE. (Left) Validation perplexity on 124M Llama pretraining. The clipped variant underperforms AMUSE, with the gap widening later in training. (Right) Evolution of β_t . While both methods reach similar large values, AMUSE continues to increase β_t , whereas the clipped variant saturates to 0.95.

As shown in Figure 25, the clipped schedule performs worse than AMUSE, and the gap increases later in training. This indicates that AMUSE benefits not only from using a large β_t , but also from continuously shifting the evaluation point toward the averaged trajectory.